Physics – Uspekhi **59** (10) 947 – 967 (2016)

REVIEWS OF TOPICAL PROBLEMS PACS numbers: **74.20. – z**, 74.20.Fg, 74.20.Mn, 74.20.Rp, 74.25.Jb, **74.62. – c**, **74.70. – b**

100th ANNIVERSARY OF THE BIRTH OF V L GINZBURG

High-temperature superconductivity in FeSe monolayers

M V Sadovskii

DOI: https://doi.org/10.3367/UFNe.2016.06.037825

Contents

Abstract. This paper reviews the basic experimental and theoretical aspects of high-temperature superconductivity in intercalated FeSe compounds and FeSe monolayer films on $SrTiO_3$ and similar substrates. The paper examines in detail the electronic structure of these systems, how it is calculated, and how the calculated results compare with ARPES experiments. It is emphasized that the reviewed systems have qualitatively different electronic spectra from the typical pattern of well-studied FeAs superconductors and explores the implications of these differences for a theoretical description of how these spectra form. Possible mechanisms of Cooper pairing in FeSe monolayers are discussed and the associated problems are examined. Because FeSe monolayer films on $SrTiO_3$ are typical Ginzburg 'sandwiches', the possibility of increasing their T_c via 'excitonic' superconductivity mechanisms is considered. It is shown that, while the classical version of this mechanism (as proposed for such systems by Allender, Bray, and Bardeen) fails to explain the observed values of T_c, the situation changes when optical phonons in $SrTiO_3$ (with energy of about 100 meV) are considered to be 'excitons'. Both the simplest possible model of T_c enhancement due to interaction with such phonons and more complex ones with dominant 'forward' scattering that explain successfully the increase in T_c compared to bulk FeSe and intercalated FeSe systems are verified. Problems related to the antiadiabatic nature of this superconductivity mechanism are also discussed.

Keywords: high-temperature superconductivity, iron chalcogenides, electronic spectrum, excitonic mechanism, electron–phonon mechanism

M V Sadovskii Institute for Electrophysics,
Ural Branch of the Russian Academy of Sciences,
ul. Amundsena 106, 620016 Ekaterinburg, Russian Federation
E-mail: sadovski@iep.uran.ru
M N Mikheev Institute for Metal Physics,
Ural Branch of the Russian Academy of Sciences,
ul. S. Kovalevskoi 18, 620290 Ekaterinburg, Russian Federation

Received 14 April 2016, revised 8 June 2016
Uspekhi Fizicheskikh Nauk **186** (10) 1035 – 1057 (2016)
DOI: 10.3367/UFNr.2016.06.037825
Translated by M V Sadovskii; edited by A Radzig

1. Introduction

The discovery of a new class of superconductors based upon iron pnictides has opened new perspectives in studies of high-temperature superconductivity. While possessing main superconducting characteristics somehow inferior to those of copper oxides (cuprates), these systems have attracted much attention from researchers, as the nature of superconductivity and other physical properties here are in many respects different from those of cuprates, while preserving many common features, which leads to hopes of a deeper understanding of the problem of high-temperature superconductivity as a whole. And this problem, which was put onto the agenda mainly due to the enthusiasm of V L Ginzburg [1–4], still remains among the central issues of the modern physics of condensed matter.

To date, the properties of iron pnictide superconductors have been rather well studied experimentally; there is also an almost overwhelmingly accepted theoretical conception of superconductivity in these systems, which is based on the idea of the leading role of pairing interactions due to exchange of (antiferro)magnetic fluctuations, which in most cases lead to $s^{\pm}$-pairing on different sheets of the Fermi surface, which appear in these *multiple band* systems. There are a number of review papers with detailed presentations of the modern experimental situation and basic theoretical concepts used in describing these systems [5–10].

The discovery of superconductivity in iron pnictides was soon followed by the discovery of similar phenomenon in iron *chalcogenide* FeSe, which even if attracted wide attention to itself it happened probably only due to the unusual simplicity of this compound, inasmuch as its superconducting characteristics (under normal conditions) were rather modest ($T_c \sim 8$ K), and its electronic structure was quite similar to that of iron pnictides. Nonetheless, this system was also thoroughly studied (cf. review [11]).

The situation with iron chalcogenides underwent a major change with the appearance of *intercalated* FeSe-based systems, where values of T_c ranging $\sim 30-40$ K were obtained and which attracted much attention because of their unusual electronic structures [12, 13]. At present, a number of such compounds are known with properties significantly different from those in traditional iron pnictides and which obviously require the elaboration of a new theoretical approach to the mechanisms of superconductivity, as the traditional picture of $s^{\pm}$-pairing for pnictides apparently does not work here.

All these problems became more acute after the experimental observation of superconductivity with $T_c \sim 80-100$ K in monolayers of FeSe (epitaxial films) grown on an $SrTiO_3$ substrate (and a number of similar compounds). At present, we can speak of a 'new frontier' in studies of high-temperature superconductivity [14].

This short review is devoted to describing the main experimental results on superconductivity in intercalated FeSe monolayers and single-layer FeSe films on substrates like $SrTiO_3$, and to discussing a number of related theoretical problems, including possible current-carrier pairing mechanisms leading to a significant enhancement of T_c. It should be said that we remain here with more questions than answers, but this is what attracts most researchers to studies of the systems discussed in this review. This field is developing very fast, and we cannot engage in a comprehensive discussion of all the available literature. Our presentation will intentionally focus on a rather elementary (general physics) level, with an intention to make it understandable to nonspecialists. The references to many important studies can be found in papers quoted below; many papers are not mentioned simply because of the limited space for the review. However, the author hopes that this review will be of interest to a wide community of *Physics Uspekhi* readers as a kind of introduction to this new field of research, especially in connection with centenary of the great physicist V L Ginzburg, whose ideas and views on the problem of high-temperature superconductivity had so much influence on everybody who is involved in this field.

2. Main systems and experiments

2.1 Intercalated FeSe-based systems

In Fig. 1a, we demonstrate schematically the simplest crystal structures of iron-based superconductors [5–11]. The common feature here is the presence of an FeAs or FeSe plane (layer), where the Fe ions form a simple square lattice, while ions of pnictogens (Pn–As) or chalcogens (Ch–Se) are placed in the centers of these squares, above and below the Fe plane in chess-board order. In Fig. 1b, the structure of this layer is shown in more detail. Actually, the electronic states of Fe ions in the FePn(Ch) plane play a decisive role in the formation of the electronic properties of these systems, including superconductivity. In this sense, these layers are quite similar to CuO_2 planes in cuprates (copper oxides), and these systems can be considered, in the first approximation, to be quasi-two-dimensional, though the anisotropy in most of them may be not so strong. Below, we shall frequently limit ourselves to such an oversimplified picture and speak about the physics of FeSe planes (monolayers).

In Fig. 1b, arrows show the direction of the spins on Fe in the antiferromagnetic structure typically realized in the stoichiometric state of FeAs-based systems [5–10], which are antiferromagnetic metals (in their ground state). Antiferromagnetic ordering is destroyed under electron or hole doping, when the superconducting phase just appears. In this sense, the phase diagrams of the systems under consideration are quite similar to those of cuprates [5–10]. These phase diagrams at present are rather well studied. In FeSe-based systems, which will be analyzed below, the character of magnetic ordering is not known so well. Because of this, as well as due to the lack of space, we shall not discuss the magnetic properties of FeSe systems much.

Notice that all the FeAs-based structures displayed in Fig. 1a constitute simple ionic–covalent crystals. The chemical formula, say, for a typical 122-system can be written out, for example, as $Ba^{+2}(Fe^{+2})_2(As^{-3})_2$. The charged FeAs layers are held together by Coulomb forces acting from surrounding ions. In bulk FeSe, the electroneutral FeSe layers are held by much weaker van der Waals interactions. This makes such a system convenient for intercalation by different atoms or molecules, which can easily enough penetrate between the FeSe layers. The chemistry of intercalation in iron selenide superconductors is discussed in detail in recent review [15].

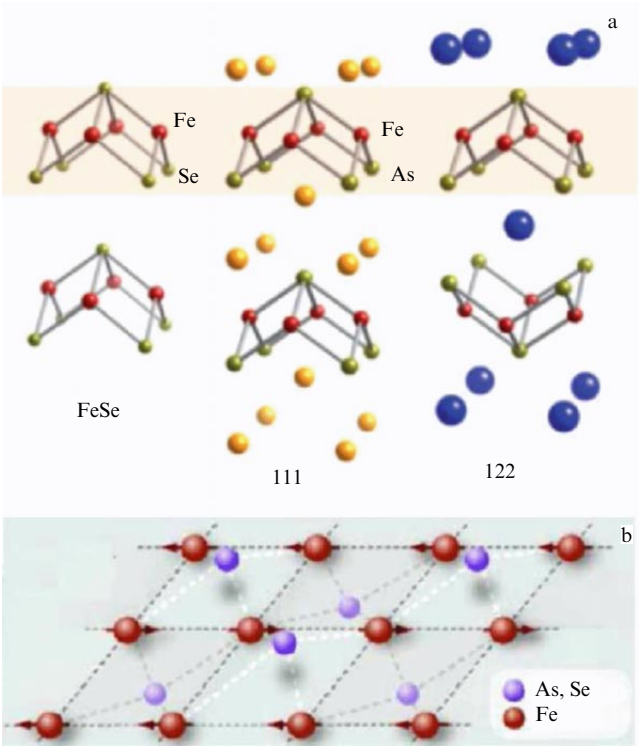

Figure 1. (Color online.) (a) Crystal structure of simplest iron-based superconductors. (b) Structure of highly conducting plane (layer) of iron ions and pnictogens (chalcogens). Arrows show directions of spins for typical ordering in the antiferromagnetic phase.

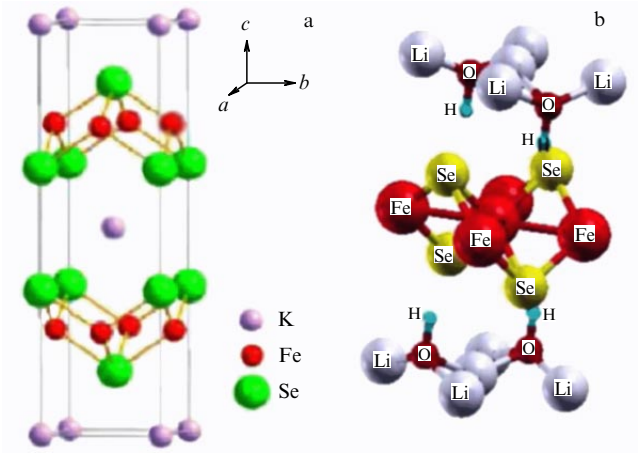

Figure 2. (Color online.) (a) Ideal ($x = 1$) crystal structure (122-type) of $K_xFe_2Se_2$ compound. (b) Ideal ($x = 0$) crystal structure of $[Li_{1-x}Fe_xOH]FeSe$ compound.

As we already noted, superconductivity in bulk FeSe, discovered immediately after high-temperature superconductivity was observed in iron pnictides, has been studied more or less in detail [11], but initially had not attracted much interest because of its similarity to superconductivity in iron pnictides and fairly low superconducting characteristics. This situation changed drastically after the discovery of high-temperature superconductivity in intercalated FeSe-based compounds and especially after the achievement of record-breaking values of T_c in single-layer FeSe films on $SrTiO_3$.

The first systems of this kind were $A_xFe_{2-y}Se_2$ (A = K, Rb, Cs) compounds, with T_c values of ~ 30 K [16, 17]. It is commonly assumed that superconductivity here is realized in a 122-like structure, shown in Fig. 2a, while real samples, studied up to now, have always been multiphased, consisting of a mesoscopic mixture of superconducting and insulating (antiferromagnetic) structures like $K_2Fe_4Se_5$, which naturally complicates the general picture. A significant further increase in T_c to values on the order of 45 K was achieved by intercalating the FeSe layers by large enough molecules in compounds like $Li_x(C_2H_8N_2)Fe_{2-y}Se_2$ [18] and $Li_x(NH_2)_y(NH_3)_{1-y}Fe_2Se_2$ [19]. The increase in T_c in these systems can be supposedly attributed to the rise of spacing between FeSe layers from 5.5 Å in bulk FeSe to ~ 7 Å in $A_xFe_{2-y}Se_2$, and to 8–11 Å in systems intercalated by large molecules, i.e., with the growth of their two-dimensional nature.

Recently, active studies have begun on the $[Li_{1-x}Fe_xOH]FeSe$ system, where T_c values of ~ 43 K were reached [20, 21] and it was possible to prepare rather good single-phase samples and single crystals. The crystal structure of this system is depicted in Fig. 2b.

An interesting discussion has developed on the nature of possible magnetic ordering on Fe ions replacing Li in intercalating LiOH layers. In Ref. [20], it was claimed that this ordering corresponds to a canted antiferromagnet. However, magnetic measurements of Ref. [21] has led to an unexpected conclusion about the *ferromagnetic* character of this ordering with the Curie temperature $T_C \sim 10$ K, i.e., much lower than the superconducting transition temperature. This conclusion was indirectly confirmed in Ref. [22] by the observation of neutron scattering on the lattice of Abrikosov vortices, supposedly induced in FeSe layers by ferromagnetic ordering of Fe spins in $Li_{1-x}Fe_xOH$ layers. At the same time, it was claimed in Ref. [23] that Mössbauer measurements on this system indicate the absence of any kind of magnetic ordering on Fe ions.

2.2 Superconductivity in the FeSe monolayer on $SrTiO_3$

A major breakthrough in studies of superconductivity in FeSe systems, as already noted above, is connected with the observation of record-breaking values of T_c in epitaxial films of the FeSe monolayer on an $SrTiO_3$ (STO) substrate [24]. These films were grown in Ref. [24] and, in most of the papers to follow, on the 001 plane of STO. The structure of these films is demonstrated in Fig. 3, where we can see, in particular, that the FeSe layer is adjacent to the TiO_2 layer on the STO surface. Notice that the lattice constant in the FeSe layer of bulk samples is 3.77 Å, while in STO it is significantly larger, being equal to 3.905 Å, so that the single-layer FeSe films are noticeably stretched, as compared to bulk FeSe, and are in a stressed state which disappears fast with the addition of the next layers. Tunneling measurements of Ref. [24] have demonstrated record values of the energy gap, while in resistance measurements the temperature of the onset superconducting transition substantially exceeded 50 K.

It should be stressed that the films under study were quite unstable in the air, so that in most of the studies resistive transitions were usually studied on films covered by amorphous Si or a number of FeTe layers, which significantly reduced the observed values of T_c. The unique *in situ* measurements of FeSe films on STO made in Ref. [25] have given record-breaking values of $T_c > 100$ K, which can be seen from the data shown in Fig. 4. So far, these results have not been confirmed by other authors, but ARPES measurements of the temperature-mediated behavior of the energy gap in such films *in situ* at present routinely demonstrate values of T_c in the interval of 65–75 K.

In films consisting of several layers of FeSe, the observed values of T_c are significantly lower than record values obtained in single-layer films [26]. Recently, single-layer FeSe films were also grown on the 110 plane of STO [27], covered up by several FeTe layers. Resistive measurements on these films (including measurements of the upper critical magnetic field H_{c2}) have given T_c values of ~ 30 K. At the same time, FeSe films grown on $BaTiO_3$ (BTO) doped with Nb (with even larger values of the lattice constant ~ 3.99 Å) have shown (in ARPES measurements) T_c values of ~ 70 K [28]. Recent paper [29] has reported the observation of record

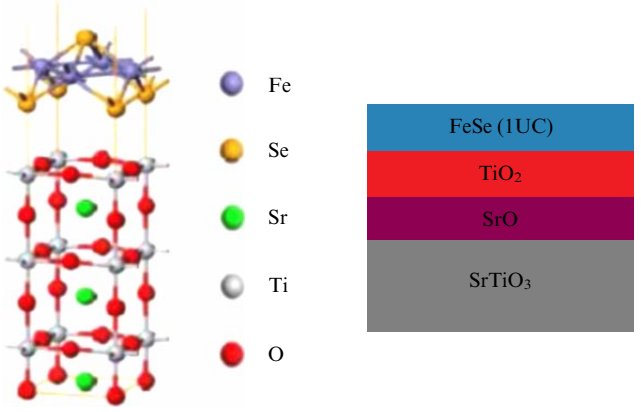

Figure 3. (Color online.) Structure of the FeSe monolayer on the $SrTiO_3$ substrate (001).

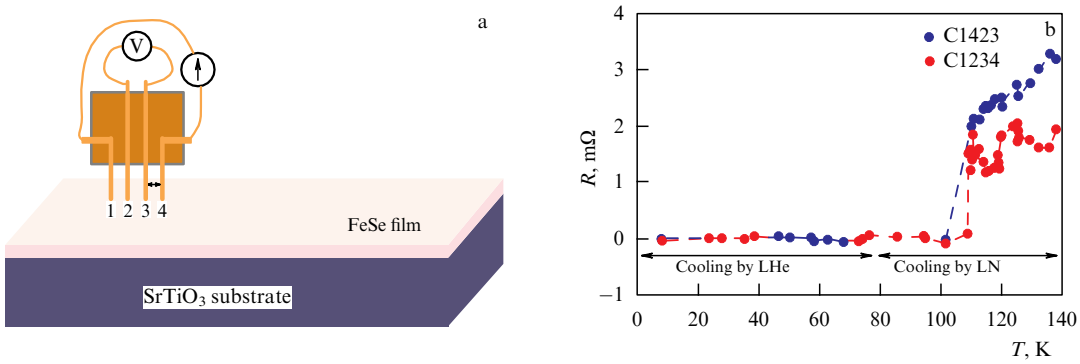

Figure 4. (Color online.) Experimental setup to measure resistance of a single-layer FeSe film on an $SrTiO_3$ substrate, and (b) temperature dependence of resistivity obtained in two samples [25].

(for FeSe systems) values of the superconducting gap (from tunneling) in FeSe monolayers on the (001) plane of TiO_2 (anatase), grown on the 001 plane of $SrTiO_3$. It was noted that the lattice constants of anatase are quite close to those of bulk FeSe, so that a FeSe film is not really stretched.

Single-layer FeSe films were also grown on a graphene substrate [30], but the T_c values of these films have not exceeded 8–10 K, characteristic of bulk FeSe, which stresses the role of substrates like $Sr(Ba)TiO_3$ possessing unique properties which may be determining in the significant enhancement of T_c.

We shall limit ourselves in this short review of the experimental situation to observations of superconductivity in FeSe monolayers in order to concentrate below on the discussion of the electronic structure and possible mechanisms explaining the record (for iron-based superconductors) values of T_c. More detailed information about experiments on this system can be found in recent review [31].

3. Electronic structure of iron–selenium systems

The electronic spectrum of iron pnictides has now been well studied both from numerical simulations based on modern energy band theory and experimentally, where the decisive role was played by angle-resolved photoemission spectroscopy (ARPES) [5–10]. As we already noted above, almost all effects of interest to us are produced by electronic states of the FeAs plane (layer), shown in Fig. 1b. The spectrum of carriers in the vicinity of the Fermi level (with a width of ~ 0.5 eV, where everything concerning the formation of a superconductive state obviously takes place) is practically determined only by d-states of Fe. Hybridization of Fe and As states according to all band structure calculations is very small. Accordingly, up to five bands (two or three hole-like and two electron-like) cross the Fermi level, forming the spectrum typical for a semimetal. A schematic diagram of Brillouin zones and Fermi surfaces is plotted in Fig. 5, and it is essentially rather simple.

In the first approximation, assuming that all As ions belong to the same plane as Fe ions, we have an elementary cell with one Fe and (square) lattice constant a (Fig. 5a). The corresponding Brillouin zone is shown in Fig. 5b. If we take into account that As ions are in fact placed above and below the Fe plane, as illustrated in Fig. 1b, the elementary cell will contain two Fe ions and the Brillouin zone is reduced by a factor of two, as shown in Fig. 5c. Two-dimensional Fermi surfaces for the case of four bands (two hole-like in the center and two electron-like at the edges or in the corners of appropriate Brillouin zones) are also schematically depicted in Fig. 5b, c.

In the narrow energy interval around the Fermi level, which is of interest to us, energy bands can be considered parabolic, so that the Hamiltonian of free carriers can be written out as [8]

$$H = \sum_{\mathbf{k},\sigma,i=\alpha_1,\alpha_2,\beta_1,\beta_2} \varepsilon^i_{\mathbf{k}} c^\dagger_{i\mathbf{k}\sigma} c_{i\mathbf{k}\sigma}\,, \tag{1}$$

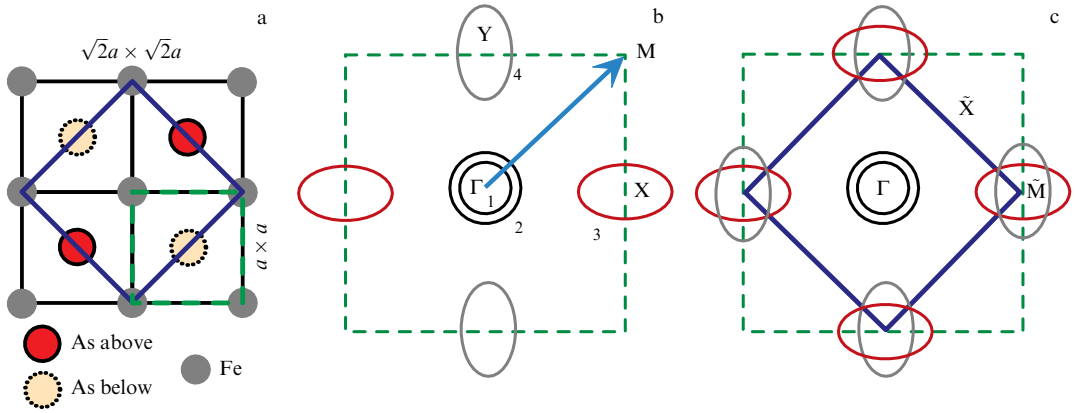

Figure 5. (Color online.) (a) Different choices of an elementary cell in the FeAs(Se) plane. (b) Brillouin zone and Fermi surfaces for the case of one Fe ion in the elementary cell. (c) Folded Brillouin zone and Fermi surfaces for the case of two Fe ions in the elementary cell.

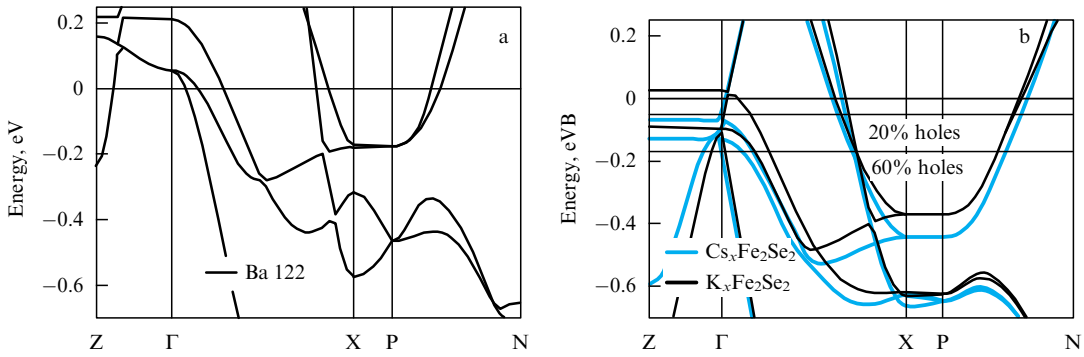

Figure 6. (a) LDA bands of Ba122 close to the Fermi level ($E = 0$) [37]. (b) LDA bands of $K_xFe_2Se_2$ (black lines) and $Cs_xFe_2Se_2$ (gray lines). Additional horizontal straight lines correspond to Fermi level positions at 20% and 60% hole doping [35].

where $c_{i\mathbf{k}\sigma}$ is the annihilation operator of an electron with momentum $\mathbf{k}$, spin σ, and band index i, while the hole α_i-band dispersions take the form

$$\varepsilon_{\mathbf{k}}^{\alpha_{1,2}} = -\frac{k^2}{2m_{1,2}} + \mu\,, \tag{2}$$

and the electron β_i-band dispersions are written out (in the coordinates of the Brillouin zone in Fig. 5b) as

$$\varepsilon_{\mathbf{k}}^{\beta_1} = \frac{(k_x - \pi/a)^2}{2m_x} + \frac{k_y^2}{2m_y} - \mu\,,$$
$$\varepsilon_{\mathbf{k}}^{\beta_2} = \frac{k_x^2}{2m_y} + \frac{(k_y - \pi/a)^2}{2m_x} - \mu\,. \tag{3}$$

More complicated band structure models valid in the vicinity of the Fermi level and in direct correspondence with the local density approximation (LDA) calculations can also be proposed (see, e.g., paper [32]), but the general, rather simple, picture of this 'standard model' of the iron pnictide spectrum remains the same. LDA + DMFT (dynamical mean-field theory) calculations [33, 34] taking into account the contribution from electron correlations show that in iron pnictides, in contrast to cuprates, their role is rather irrelevant and reduced to (actually noticeable) renormalization of the effective masses of electron and hole dispersions, as well as to the general 'compression' (reduced width) of the bands.

The presence of electron and hole Fermi surfaces with close sizes satisfying (approximately!) the 'nesting' conditions is very significant for the theories of superconducting pairing in iron pnictides, based on the decisive role of antiferromagnetic spin fluctuations [8]. Below, we shall see that the electronic spectrum and Fermi surfaces in Fe chalcogenides are significantly different from the qualitative pattern presented above, which poses new (and far from solved) problems for explaining the microscopic mechanism of superconductivity in these systems.

3.1 $A_xFe_{2-y}Se_2$ system

LDA calculations of the electronic spectrum of the $A_xFe_{2-y}Se_2$ (A = K, Cs) system were performed immediately after its discovery in experiment [35, 36]. Rather unexpectedly, this spectrum was found to be qualitatively different from the spectrum of bulk FeSe and the spectra of all the known FeAs systems. In Fig. 6, we compare the spectrum of $BaFe_2As_2$ (Ba122) [37], which is typical for all FeSe-based

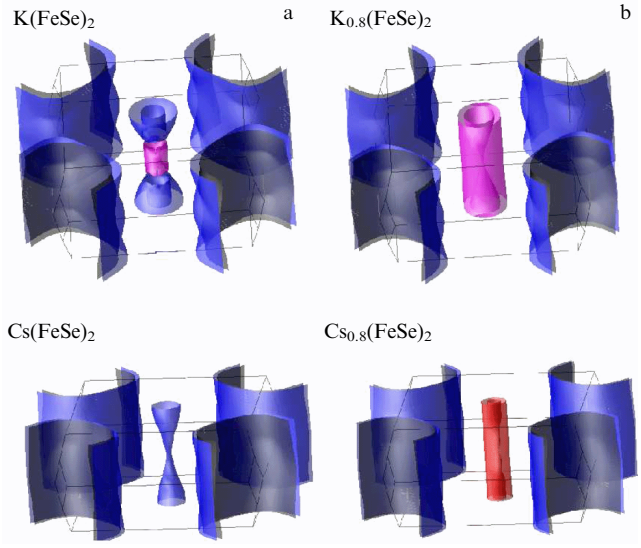

Figure 7. Fermi surfaces of $A_xFe_2Se_2$ (A = K, Cs) for the stoichiometric composition (a) and for the case of 20% hole doping (b) [35].

systems, and the $A_xFe_{2-y}Se_2$ (A = K, Cs) spectrum obtained in Ref. [5]. We can see the clear difference between these spectra in the vicinity of the Fermi level.

In Fig. 7, we exhibit the Fermi surfaces calculated in Ref. [35] for two typical compositions of $A_xFe_{2-y}Se_2$ (A = K, Cs). It can be seen that these are quite distinct from the Fermi surfaces of FeAs systems — in the center of the Brillouin zone there are only small (electron-like!) Fermi surfaces, while electron-like cylinders at the corners of the Brillouin zone are much larger. The shape of Fermi surfaces typical for bulk FeSe- and FeAs-based systems is reproduced only for much larger (unreachable) hole doping levels [38].

This shape of the Fermi surfaces in $A_xFe_{2-y}Se_2$ compounds was soon confirmed by ARPES experiments. As an example, we show in Fig. 8 ARPES data from Ref. [38], which are in obvious qualitative correspondence with LDA calculated results [35, 36].

It is seen that in this system we cannot speak of any, even approximate, 'nesting' properties of electron-like and hole-like Fermi surfaces, while it is precisely these properties that form the basis of most theoretical approaches to a microscopic description of FeAs-based systems [8], where the 'nesting' of electron-like and hole-like Fermi surfaces leads to a picture of well-developed spin fluctuations which make up the main mechanism of pairing interaction.

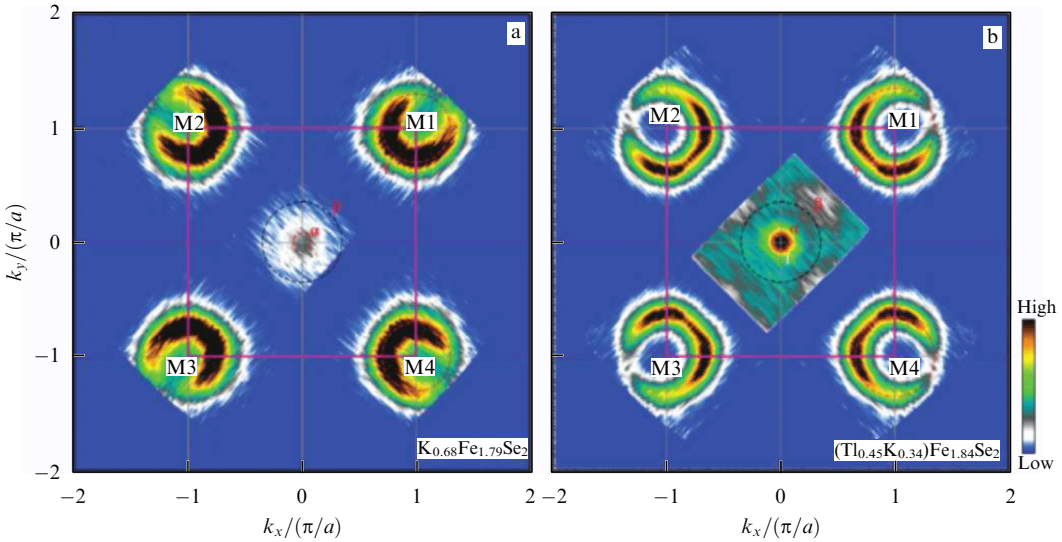

Figure 8. (Color online.) ARPES Fermi surfaces of (a) $K_{0.68}Fe_{1.79}Se_2$ ($T_c = 32$ K) and (b) $Tl_{0.45}K_{0.34}Fe_{1.84}Se_2$ ($T_c = 28$ K) [38].

LDA + DMFT calculations of $K_{1-x}Fe_{2-y}Se_2$ for different doping levels were performed in Refs [39, 40]. In this regard, besides the standard LDA + DMFT procedure, we also used the modified LDA′ + DMFT approach developed by us in Refs [41, 42], which allows, in our opinion, a more consistent solution to the 'double-counting' problem of Coulomb interactions in LDA + DMFT. For DMFT calculations, we chose $U = 3.75$ eV and $J = 0.56$ eV as the values of the Coulomb and exchange electron interactions in the 3d shell of Fe. As *impurity solver*, we have used the Quantum Monte Carlo (QMC) method. The results of these calculations were directly compared with the ARPES data from Refs [43, 44].

It can be seen that the correlation effects for a $K_{1-x}Fe_{2-y}Se_2$ system play a rather significant role. They lead to a noticeable change in LDA dispersions. In contrast to iron arsenides, where the quasiparticle bands close to the Fermi level remain well-defined, in $K_{1-x}Fe_{2-y}Se_2$ compounds in the vicinity of the Fermi level we observe rather strong suppression of quasiparticle bands. This reflects the fact that correlation effects in this system are stronger than in iron arsenides. The value of correlation renormalization (correlation narrowing) of the bands close to the Fermi level is given by the factor of 4 to 5, while in iron arsenides this factor is usually on the order of 2 to 3 for the same values of interaction parameters.

Results of these calculations are in general qualitative agreement with the ARPES data of Refs [43, 44], which also demonstrate the strong damping of quasiparticles in the immediate vicinity of the Fermi level and stronger renormalization of effective masses than in FeAs systems. At the same time, our calculations do not reveal the formation of an unusually 'shallow' (~ 0.05 eV below the Fermi level) electron-like band at the X point in the Brillouin zone, which was observed in ARPES experiments.

3.2 $[Li_{1-x}Fe_xOH]FeSe$ system

In Ref. [45], we performed LDA calculations of the stoichiometric LiOHFeSe compound; the appropriate results for energy dispersions are given in Fig. 9a. On first sight, the energy spectrum of this system is quite analogous to the spectra of the majority of FeAs systems and that of bulk FeSe. In particular, the main contribution to the density of states in a rather wide energy region around the Fermi level comes from d-states of Fe, while the Fermi surfaces qualitatively have the same shape as in the majority of Fe-based superconductors. However, this impression is wrong — in the real $[Li_{0.8}Fe_{0.2}OH]FeSe$ superconductor, the partial substitution of Fe for Li in intercalating LiOH layers leads to significant *electron* doping, so that the Fermi level goes upward in energy (as opposed to the stoichiometric case) by 0.15–0.2 eV. Whereas, as is clear from Fig. 9a, hole-like bands in the vicinity of point Γ move below the Fermi level, so that hole-like cylinders of the Fermi surface just vanish. The general shape of the Fermi surfaces for such an electron doping level, following from LDA calculations, is illustrated in Fig. 9b, and it has much in common with similar results for the $A_xFe_{2-y}Se_2$ system (cf. Fig. 7). This conclusion is confirmed by direct ARPES experiments [46], the results of which are displayed in Fig. 9c.

In particular, it can be seen from Fig. 9b that Fermi surfaces consist mainly of electron-like cylinders around points M, while the Fermi surface in the vicinity of point Γ is either absent or quite small. In any case, for this system there are no 'nesting' properties between electron and hole surfaces in any sense. Electronic dispersions determined from ARPES are quite similar to corresponding dispersions measured in Refs [43, 44] for the $K_{1-x}Fe_{2-y}Se_2$ system. These are qualitatively similar to dispersions obtained in LDA calculations taking into account the strong enough correlation narrowing of bands (the compression factor is actually different for various bands, as was shown by LDA + DMFT calculations in Refs [39, 40]). At the same time, the origin of an unusually 'shallow' electronic band ~ 0.05 eV deep close to point M remains unclear. To explain this peculiarity we need invoking of unusually strong correlation narrowing (while conserving the diameter of electron-like cylinders around the M point, which practically coincides with the results of LDA calculations), which is difficult to obtain from LDA + DMFT calculations.

In Ref. [45], local spin-density approximation (LSDA) calculations of exchange integrals were performed for typical configurations of Fe ions, replacing Li in LiOH layers. For the most probable configuration, leading to magnetic order-

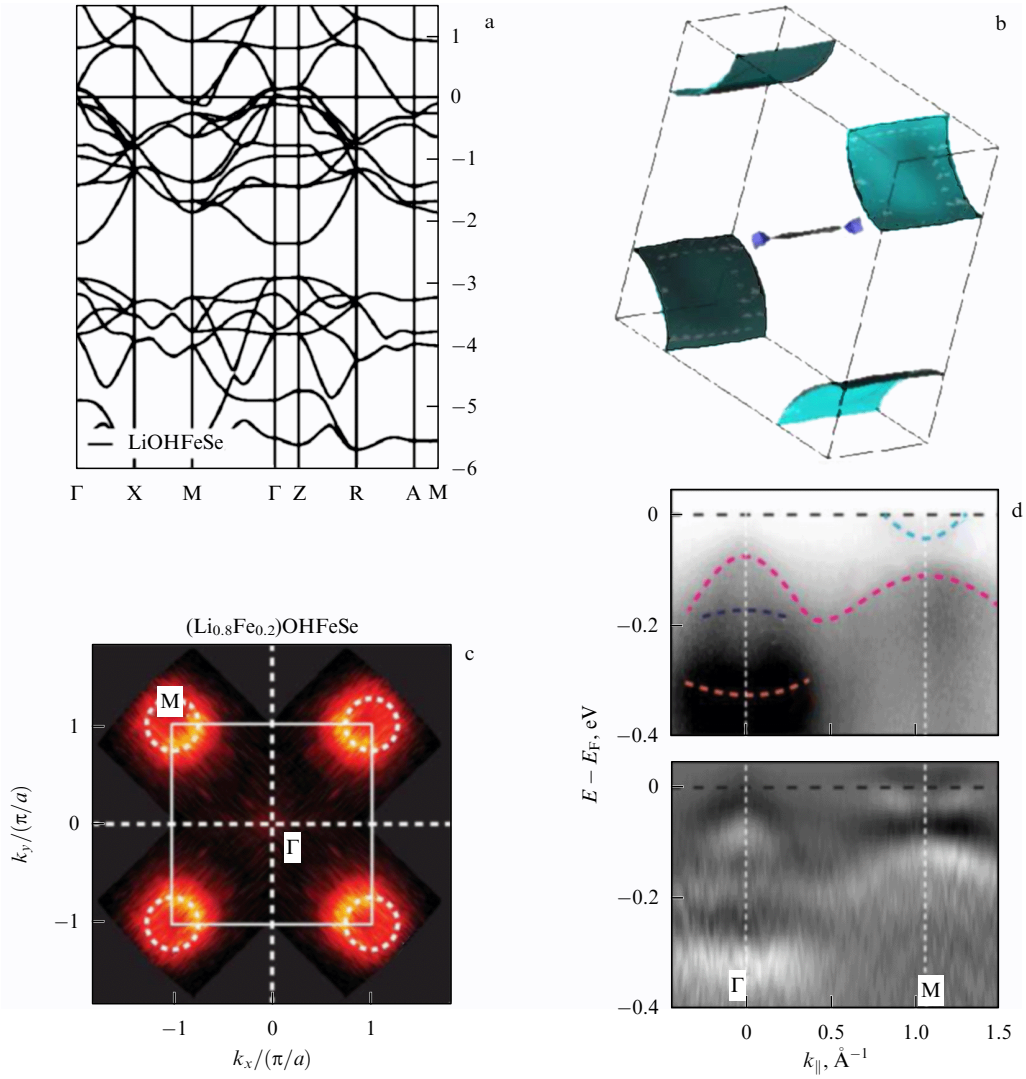

Figure 9. (Color online.) (a) LDA bands of LiOHFeSe (Fermi level at $E = 0$) [45]. (b) Fermi surface of LiOHFeSe corresponding to a doping level of 0.3 electrons per unit cell. (c) ARPES Fermi surfaces of $[Li_{0.8}Fe_{0.2}OH]FeSe$ [46]. (d) ARPES bands close to the Fermi level in $[Li_{0.8}Fe_{0.2}OH]$ FeSe [46]. Dashed lines in figure (d) indicate the positions of spectral density maxima defining electron dispersions.

ing, the positive (ferromagnetic) sign of exchange interaction was obtained and the simplest estimate of the Curie temperature has given the value of $T_C \approx 10$ K, in excellent agreement with the experimental data of Refs [21, 22], which reported the observation of ferromagnetic ordering on Fe in LiOH layers. At the same time, as we mentioned in Section 2.1, the other experiments had cast some doubts on this conclusion.

3.3 FeSe monolayer

LDA calculations of spectra of a single-layer FeSe can be done in the standard way [47]. The results of such calculations are represented in Fig. 10a. It is seen that the spectrum looks typical for FeAs systems and bulk FeSe, which was discussed in detail above. However, the ARPES experiments [48–50] showed convincingly that this is not so. In a monolayer of FeSe on STO, only electron-like Fermi surfaces are observed around M points in the Brillouin zone, while hole-like sheets around point Γ (at the zone center) are just absent. An example of this type of data is exhibited in Fig. 11a [48]. Thus, similarly to the case of intercalated FeSe systems, any kind of 'nesting' properties are lacking here. The apparent contradiction with the results of LDA calculations has a simple qualitative explanation — the observed Fermi surfaces can be easily obtained assuming that the system is electron-doped, so that the Fermi level moves upward in energy by $\sim 0.2-0.25$ eV, as shown by the red horizontal line in Fig. 10a. This corresponds to the doping level on the order of 0.15–0.20 electrons per Fe ion.

Strictly speaking, the origin of this doping remains unclear, but there is a general consensus that it is related to the formation of oxygen vacancies in $SrTiO_3$ substrate (in TiO_2 layer), appearing during different technological operations (annealing, etching, etc.) used during the growth of the films under study. It should be noted that the formation of electron gas at the interface with $SrTiO_3$ is well known and has been studied for a rather long time [51]. However, for the FeSe/STO system of interest to us, this problem has not been studied in any detail (cf., though, with Refs [52, 53]).

The influence of electron correlations on the spectrum of a single-layer FeSe is relatively weak. In Fig. 10b, we show the results of LDA + DMFT calculations for the case of a properly shifted (by electron doping) Fermi level [47]. DMFT calculations were performed for the values of the Coulomb and

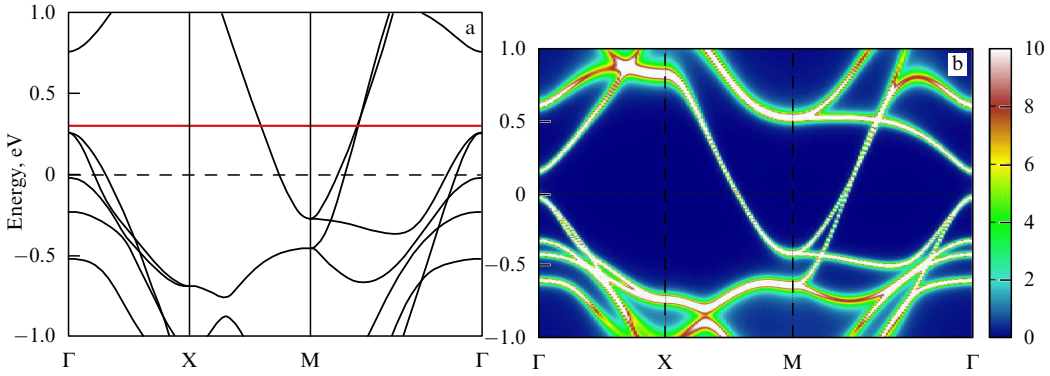

Figure 10. (Color online.) (a) LDA bands of a single-layer FeSe close to the Fermi level ($E = 0$). Horizontal red line denotes the approximate position of the Fermi level, corresponding to an electron doping level bringing about the Fermi surfaces observed in ARPES experiments [47]. (b) LDA + DMFT-calculated bands of a single-layer FeSe close to the Fermi level shifted by electron doping [47].

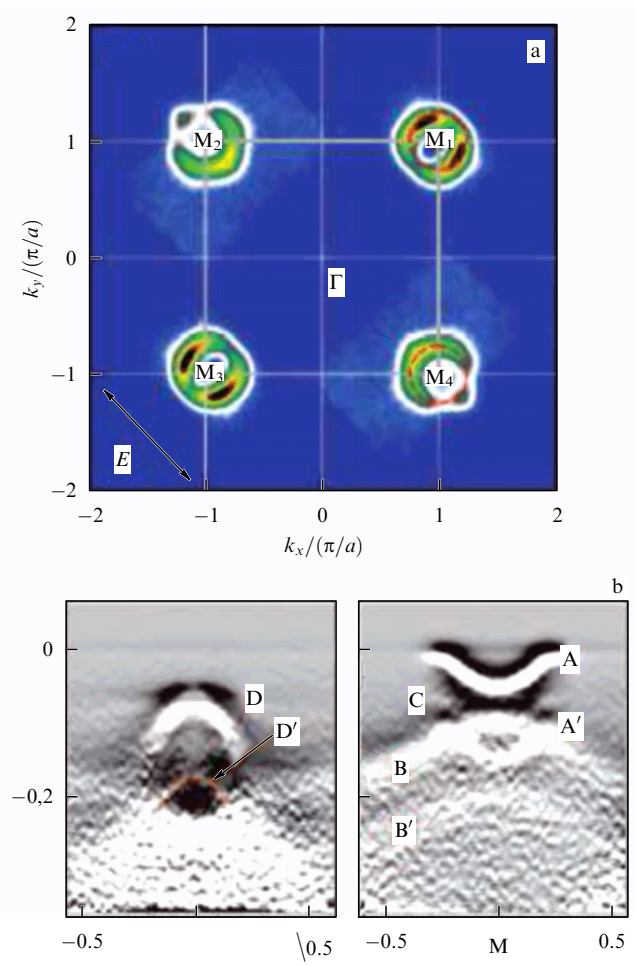

Figure 11. (Color online.) (a) ARPES Fermi surface of a single-layer FeSe [48]. (b) ARPES bands of an FeSe single layer close to the Fermi level [49].

exchange (Hund-like) interaction energies of electrons in the 3d shell of Fe, taken as $U = 3.5$ eV and $J = 0.85$ eV. As the *impurity solver*, we have used here the continuous–time quantum Monte Carlo (CT–QMC) method, and the dimensionless inverse temperature was taken to be $\beta = 40$. We can see that the spectrum is only weakly renormalized by correlations and conserves its LDA-like shape with a rather low bandwidth compression factor of ~ 1.3.

Electronic dispersions in FeSe monolayer films were measured by ARPES in a number of studies, e.g., in Refs [28, 49]. The results of Ref. [49] are presented in Fig. 11b. They are in agreement with data obtained in other papers and are, in general, analogous to the similar results obtained for intercalated FeSe systems (cf., e.g., Fig. 9c). By and large, these data are also qualitatively similar to the LDA + DMFT results, but the quantitative agreement is absent. In particular, ARPES experiments clearly demonstrate the presence of an unusually 'shallow' electron-like band at the point M with a Fermi energy of ~ 0.05 eV, while in theoretical calculations this band is almost an order of magnitude 'deeper'.

It should also be noted that the authors of Ref. [49] observed for the first time that a 'shadow' electron-like band exists at the point M, which lies about 100 meV below the main band and is a kind of a 'replica' of such a band. This band is clearly seen in Fig. 11b. Such a shadow band is absent in band structure calculations. The nature of this band and its possible significance for high-temperature superconductivity in FeSe monolayers on STO will be discussed in some detail below, in connection with possible mechanisms for increasing T_c.

As we noted above, the electron doping level of FeSe monolayers on STO is a rather poorly controlled parameter. However, in a number of papers, using different procedures of film annealing *in situ*, the authors successfully conducted ARPES experiments on samples with different doping levels [54, 55]. These experiments allowed some kind of phase diagrams for the FeSe/STO system to be obtained. In particular, a series of samples was demonstrated in Ref. [54] with consequent transitions from the topology of the Fermi surface typical of FeAs systems and bulk FeSe (with Fermi surface sheets around the point Γ in the center of the Brillouin zone) to the topology of Fermi surface sheets around point M. It was shown that high-T_c superconductivity appears only in samples without central Fermi surface sheets, whereas samples with the typical Fermi surface topology remain in the normal (N) phase. These results are given schematically in Fig. 12a. The presence of superconductivity was evidenced from ARPES measurements of the energy gap at the Fermi level, and T_c was derived from the temperature dependence of the gap.

In Ref. [55], similar measurements were done with electron concentration controlled by measurements of the area of electron pockets of the Fermi surface around the M points. The phase diagram obtained is plotted in Fig. 12b, where we see an insulating (antiferromagnetic?) phase at low doping levels, and a superconducting phase appearing at dopings exceeding the critical value of ~ 0.09, corresponding to the quantum critical point. These conclusions are also

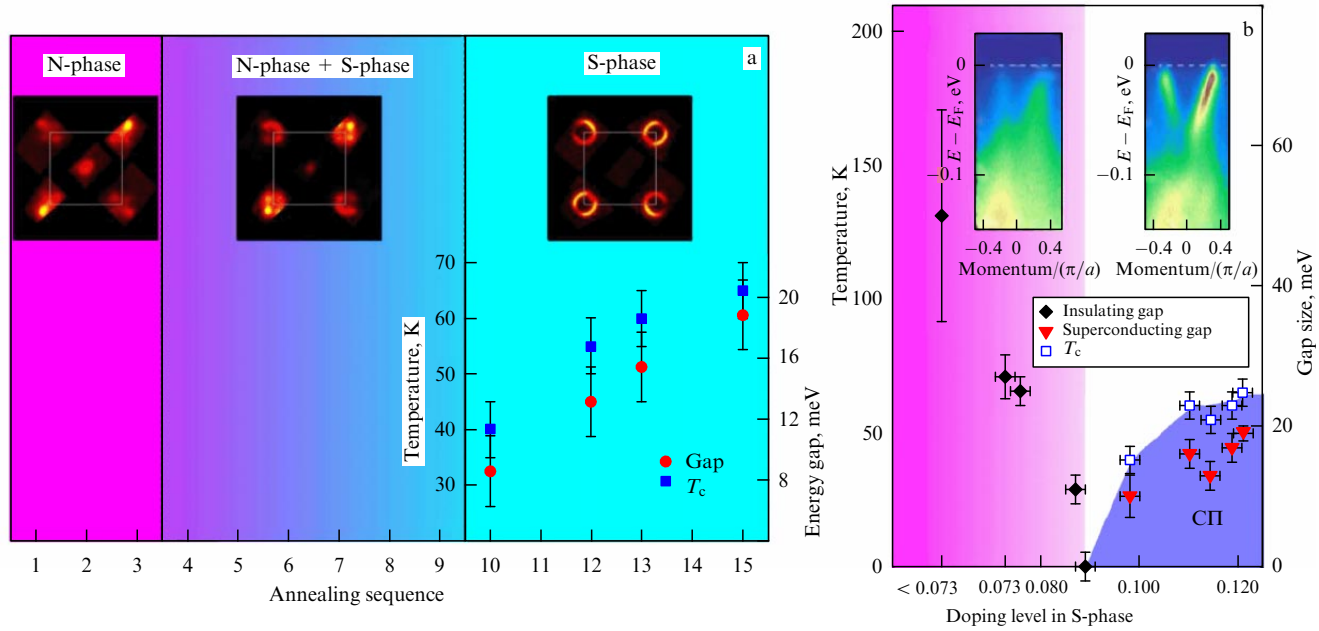

Figure 12. (Color online.) Phase diagram of an FeSe single layer on $SrTiO_3$. (a) Schematic phase diagram obtained in Ref. [54] on a series of samples with different electron dopings. Also shown are corresponding ARPES Fermi surfaces and, in the superconducting (S) phase, ARPES-measured values of the superconducting gap and T_c. (b) Phase diagram obtained from ARPES measurements in Ref. [55] and demonstrating the existence of insulating and superconducting phases. The values of superconducting and insulating gaps were also obtained from ARPES measurements.

based on ARPES measurements of superconducting and insulating energy gaps in the spectrum and their temperature dependences.

It is obvious that the results of Refs [54, 55] somewhat contradict each other, notably, the nature of the insulating phase observed in paper [55] remains unclear.

4. Possible mechanisms of T_c enhancement in iron–selenium monolayers

4.1 Correlation between T_c and the density of states

Let us now start discussing the mechanisms of high-temperature superconductivity in the systems under consideration. Concerning FeAs-based superconductors, there is a general consensus in the literature. The electron–phonon mechanism of Cooper pairing is considered to be insufficient in explaining the high values of T_c in these systems [5], and the preferable mechanism is assumed to be pairing due to the exchange of antiferromagnetic fluctuations. The repulsive nature of this interaction leads to a picture of $s^{\pm}$-pairing with different signs of superconducting order parameter (gap) Δ on hole-like (around the point Γ in the center of the Brillouin zone) and electron-like (around points M in the corners of the zone) sheets of the Fermi surface [8]. However, when we consider systems based on FeSe monolayers, this picture obviously becomes inconsistent — the observed topology of Fermi surfaces with a complete absence of any 'nesting' electron-like and hole-like sheets or even with a total absence of hole-like Fermi surfaces clearly contradicts this picture. There is simply no obvious way to produce well-developed spin (antiferromagnetic) fluctuations. Thus, we shall start with an elementary analysis based on the simple Bardeen–Cooper–Schrieffer (BCS) model.

In Ref. [56], an interesting empirical dependence was discovered between the superconducting transition temperature T_c in FeAs and FeSe systems and the height of anion (As or Se) position Δz_a above the Fe plane (layer) (cf. Fig. 1). A sharp maximum of T_c was observed for systems with $\Delta z_a \sim 1.37$ Å. In Refs [12, 57], we presented the results of systematic LDA calculations of the total density of states at the Fermi level, $N(E_F)$, for a wide choice of (stoichiometric) FeAs- and FeSe-based systems with different values of Δz_a (cf. Table 1). The obtained nonmonotone dependence of the density of states on Δz_a, shown in Fig. 13 (dots), which is determined by hybridization effects is, in principle, sufficient for explaining the corresponding dependence of T_c.

The appropriate dependence of T_c on Δz_a can be easily estimated along the lines of the elementary BCS model, applying the usual expression $T_c = 1.14\omega_D \times \exp(-1/\lambda)$ and taking into account that $N(E_F)$ directly enters dimensionless pairing interaction constant $\lambda = gN(E_F)$ (where g is the corresponding dimensional coupling constant). Taking the

Table 1. Total LDA-calculated density of states $N(E_F)$ and the values of T_c for iron-based superconductors.

System	Δz_a, Å	$N(E_F)$/cell/eV	T_c^{BCS}, K	T_c^{exp}, K
LaOFeP	1.130	2.28	3.2	6.6
$Sr_4Sc_2O_6Fe_2P_2$	1.200	3.24	19	17
LaOFeAs	1.320	4.13	36	28
SmOFeAs	1.354	4.96	54	54
CeOFeAs	1.351	4.66	48	41
NdOFeAs	1.367	4.78	50	53
TbOFeAs	1.373	4.85	52	54
SrFFeAs	1.370	4.26	38	36
$BaFe_2As_2$	1.371	4.22	38	38
CaFFeAs	1.420	4.04	34	36
$CsFe_2Se_2$	1.435	3.6	29	27
KFe_2Se_2	1.45	3.94	34	31
LiOHFeSe	1.485	4.14	36	43
LiFeAs	1.505	3.86	31	18
FeSe	1.650	2.02	3	8

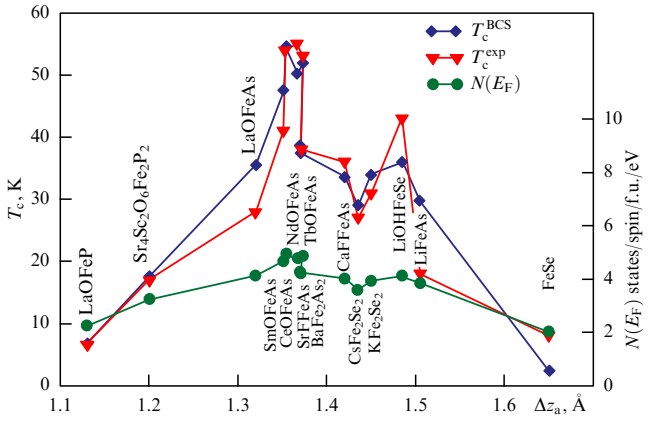

Figure 13. LDA-calculated values of the density of states $N(E_F)$ (dots, right axis) at the Fermi level and superconductor critical temperature T_c (left axis) obtained from elementary BCS type estimates, T_c^{BCS} (stars), and experimental values of T_c — T_c^{exp} (triangles) as functions of anion height Δz_a over the Fe layer for different iron-based superconductors.

rather arbitrary value of $\omega_D = 350$ K (which may be related to the characteristic value of phonon frequencies in FeAs systems [5]), we can determine the value of g fitting the experimental value of T_c, e.g., for the Ba122 system (~ 38 K), which gives $\lambda = 0.43$. Fixing this value of g, we can easily recalculate the values of T_c for all other systems just taking appropriate values of the density of states from LDA calculations (cf. Fig. 13). The relevant values of T_c given in Table 1 and plotted in Fig. 13 (stars) are in very reasonable agreement with the experimental values marked in the same figure (triangles), which are also compiled in Table 1.

FeSe-based systems just fit, in general, this dependence. This can be seen from the data of Table 1 and Fig. 13. For example, for the $[Li_{1-x}Fe_xOH]FeSe$ system, the calculated value of the density of states for stoichiometric composition LiOHFeSe is $N(E_F) = 4.14$ states/cell/eV, and the elementary estimate of T_c yields $T_c = 36$ K, which is somehow lower than the experimental value of $T_c^{exp} = 43$ K. However, introducing Fe into LiOH layers shifts the Fermi level, so that it moves to a higher value of $N(E_F)$ (4.55 states/cell/eV), leading to the relevant growth of T_c up to 45 K, which is very close to the experimental value [45].

It should be stressed that the above-given rough estimates do not necessarily mean that we assign an electron–phonon Cooper pairing mechanism to these systems, and ω_D in the BCS expression can just be considered a characteristic frequency of any kind of boson excitations responsible for pairing (e.g., magnetic fluctuations). These results simply show that there is an obvious correlation between experimental values of T_c and the value of the total density of states at the Fermi level obtained via band structure calculations for stoichiometric (!) compositions of FeAs- and FeSe-based compounds. Similar findings can be arrived at using more complicated expressions for T_c like the McMillan or Allen–Dynes formulas [57].

At the same time, for a single-layer FeSe, LDA calculations produce the value of $N(E_F) \approx 2$ states/cell/eV, which is practically the same as for bulk FeSe and changes weakly with electron doping (Fermi level shift) [47]. The corresponding elementary estimate of T_c does not produce values higher than 8 K, so the appearance of high T_c values in this case cannot be explained from analogous simple considerations.

However, there are a number of experimental papers where a significant increase in T_c was reported up to values on the order of 40 K in bulk crystals and multilayer films of FeSe under their electron doping achieved by covering the surface of FeSe with alkali metal (sodium) atoms [58–60]. It is possible that this treatment has led to the intercalation of FeSe layers by an alkali metal, so that these systems were transformed into an analogue of intercalated FeSe-based systems, similar to those discussed above, and the growth of T_c was related to an increase in $N(E_F)$. This point of view is confirmed by calculations presented in Ref. [61]. However, the growth of T_c to values > 40 K was also achieved in a number of papers by doping FeSe induced by a strong external electric field (at the gate) in field-effects transistor structures [62–64], where a similar explanation seems less probable.

4.2 Multiple bands picture of superconductivity

A basic feature of the electronic spectrum of iron pnictide and chalcogenide superconductors is its multiple band character: in general, the Fermi level is crossed by several bands formed with d-states of Fe, so that several sheets (pockets) appear on the Fermi surface (electron- and hole-like) [5, 8, 10]. In the superconducting state, an energy gap can open on each of these sheets and the values of these gaps can be quite different from each other [5, 10]. Thus, an elementary description of superconductivity based on the single-band BCS model used in the previous section is in fact oversimplified. Below, following mainly Refs [65, 66], we shall briefly describe the multiple-band formulation of the BCS model as applied to Fe-based superconductors.

Let us consider a simplified version of the electronic structure (Fermi surfaces) of the Fe square lattice, shown in Fig. 5b, with two hole-like pockets around point Γ and two electron-like pockets around points X and Y (in the Brillouin zone for the square lattice with one Fe ion per unit cell). Let Δ_i denote the superconducting order parameter (energy gap) on the ith sheet (pocket) of the Fermi surface ($i = 1, 2, 3, 4$ in Fig. 5b). The value of Δ_i is determined by the self-consistency equation for the corresponding anomalous Green's function in Gorkov's system of equations [65].

Pairing interaction in the multiple-band BCS model can be written out in the matrix form

$$\hat{V} = \begin{pmatrix} u & w & t & t \\ w & u' & t' & t' \\ t & t' & \lambda & \mu \\ t & t' & \mu & \lambda \end{pmatrix}, \tag{4}$$

where matrix elements $V^{i,j}$ define intraband and interband coupling constants. For example, $\lambda = V^{eX,eX} = V^{eY,eY}$ determines the pairing interaction on the same electron-like pocket at the point X or Y, while $\mu = V^{eX,eY}$ connects electrons on different pockets at points X and Y. Constants $u = V^{h1,h1}$, $u' = V^{h2,h2}$, and $w = V^{h1,h2}$ characterize BCS interaction on hole-like pockets — the smaller one (h1) and larger one (h2) — and between them, while $t = V^{h,eX} = V^{h,eY}$ pairs electrons at points X and Γ.

For the superconducting transition temperature, the standard BCS type expression appears:

$$T_c = \frac{2\gamma\omega_c}{\pi} \exp\left(-\frac{1}{g_{eff}}\right), \quad \gamma \approx 1.78, \tag{5}$$

where ω_c is the usual cut-off parameter in the Cooper channel (for simplicity, we assume that this parameter is the same for

all pairing interactions, while the generalization for, say, two characteristic cut-off frequencies is rather direct [67]), and $g_{\rm eff}$ stands for an *effective* pairing constant determined from the solvability condition for a system of linearized gap equations:

$$g_{\rm eff}\Delta_i = \sum_j g_{ij}\Delta_j\,, \tag{6}$$

where

$$g_{ij} \equiv -V^{i,j}\nu_j\,, \quad g_{\rm eff}^{-1} = \ln\frac{2\gamma}{\pi}\frac{\omega_{\rm c}}{T_{\rm c}} \tag{7}$$

is the matrix of dimensionless pairing constants g_{ij} determined by the products of matrix elements (4) and *partial* densities of states on different Fermi surface pockets, and ν_j denotes the density of states per spin projection on the jth pocket (cylinder).

From the symmetry arguments it is clear that $\nu_3 = \nu_4$, so that the system of equations (6) can produce two types of solutions [65]:

(1) corresponding to $d_{x^2-y^2}$-pairing, when the gaps on different sheets at points X and Y differ by sign, while gaps on hole-pockets are equal to zero:

$$\Delta_1 = \Delta_2 = 0\,, \qquad \Delta_3 = -\Delta_4 = \Delta\,, \tag{8}$$

or, as a special case, when relevant pockets are just absent;

(2) corresponding to so-called $s^{\pm}$-pairing, when gaps at points X and Y are equal: $\Delta_3 = \Delta_4$, while gaps on Fermi surface pockets surrounding point Γ have different signs in the presence of *repulsive* interaction between electron and hole pockets — $t > 0$, and usual s-wave pairing, when gaps on electron and hole pockets have the same sign in the presence of attraction — $t < 0$.

All these variants are qualitatively demonstrated in Fig. 14.

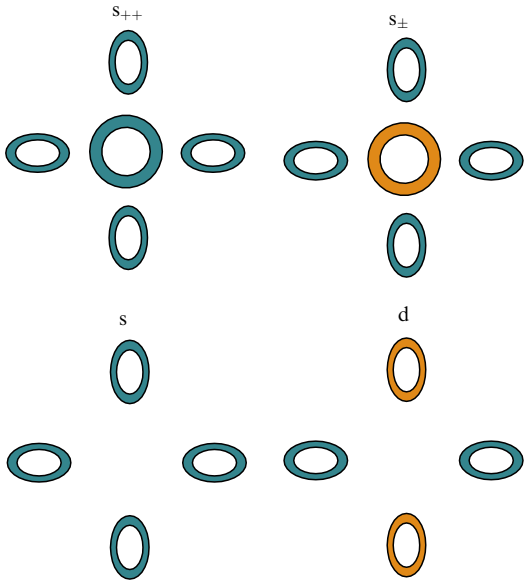

Figure 14. Main types of pairing in multiple-band scheme for superconductivity in FeAs- and FeS-based systems. Different colors mark different signs of superconducting gaps.

In the first case, we obtain the following expression for the effective pairing constant

$$g_{\rm eff} = (\mu - \lambda)\,\nu_3\,. \tag{9}$$

In the second case, we have $\Delta_3 = \Delta_4$ and $\nu_3 = \nu_4$, so that the two equations in set (6) just coincide and instead of expressions (4), (7) the coupling matrix 3×3 of the following form appears:

$$-\hat{g} = \begin{pmatrix} u\nu_1 & w\nu_2 & 2t\nu_3 \\ w\nu_1 & u'\nu_2 & 2t'\nu_3 \\ t\nu_1 & t'\nu_2 & 2\bar{\lambda}\nu_3 \end{pmatrix}, \tag{10}$$

where $\bar{\lambda} = (\lambda + \mu)/2$, and the solution to a set of equations (6) reduces to the standard procedure of finding the eigenvalues (and eigenvectors) for a matrix of dimensionless coupling constants g_{ij} (10), which are defined by the cubic secular equation

$$\mathrm{Det}\,(g_{ij} - g_{\rm eff}\delta_{ij}) = 0\,. \tag{11}$$

The physical solution is determined by the maximum positive value of $g_{\rm eff}$, which gives, in turn, the maximum value of $T_{\rm c}$. Eigenvectors of the problem determine here the ratios of the gaps Δ_i on different sheets of the Fermi surface for $T \to T_{\rm c}$. Temperature dependences of energy gaps for $T < T_{\rm c}$ can be found by solving the set of generalized BCS equations:

$$\Delta_i = \sum_j g_{ij}\Delta_j \int_0^{\omega_{\rm c}} {\rm d}\xi\, \frac{\tanh\left[\sqrt{\xi^2 + \Delta_j^2}/(2T)\right]}{\sqrt{\xi^2 + \Delta_j^2}}\,. \tag{12}$$

As $T \to 0$, these equations reduce to

$$\Delta_i = \sum_j g_{ij}\Delta_j F\left(\frac{\Delta_j}{\omega_{\rm c}}\right), \; F(x) = \ln\left(\frac{1 + \sqrt{1 + x^2}}{|x|}\right). \tag{13}$$

This analysis makes it clear that the value of $T_{\rm c}$ (effective pairing constant) in multiple-band system is determined, in general, not only by the value of the total density of states at the Fermi level (multiplied by the single dimensional coupling constant), but also by a rather complicated combination of several coupling constants, multiplied by partial densities of states for different bands. It is now becoming obvious that the multiple-band structure of the spectrum can lead to the growth of $T_{\rm c}$ by itself, reasonably enhancing the effective pairing constant in formula (5) [66]. To understand the essence of this effect, it is useful to analyze simple limiting cases.

Let a matrix of dimensionless coupling constants be diagonal (i.e., there are only intraband pairing interactions):

$$\hat{g} = \begin{pmatrix} g_1 & 0 & 0 & 0 \\ 0 & g_2 & 0 & 0 \\ 0 & 0 & g_3 & 0 \\ 0 & 0 & 0 & g_3 \end{pmatrix}. \tag{14}$$

Then, obviously, $g_{\rm eff} = \max\{g_i\}$, while $T_{\rm c}$ is determined by the density of states and pairing interaction on the single (and in this sense dominating) pocket of the Fermi surface.

Let us consider, in some sense, the opposite case, when all intraband and interband interactions in matrix (4) are the same and also all partial densities of states are just equal.

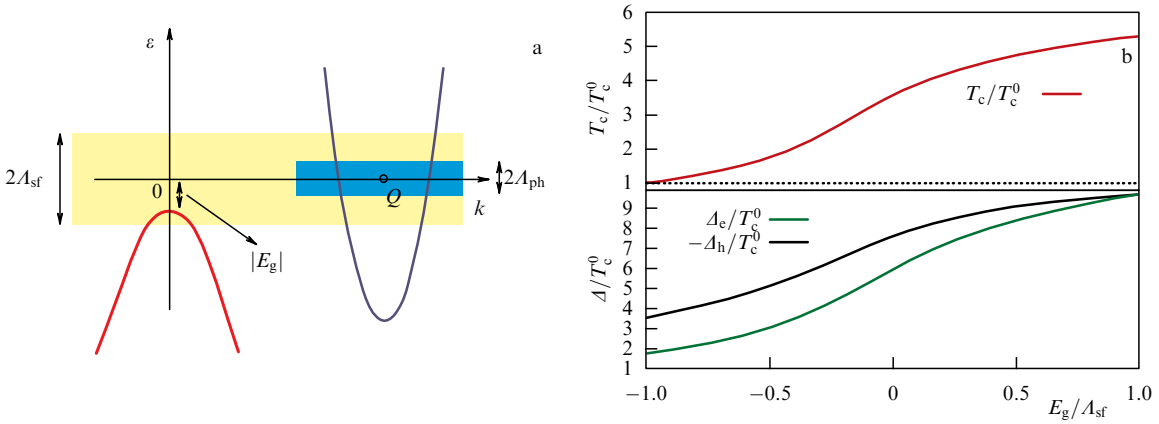

Figure 15. (Color online.) (a) Typical band structure of FeAs- and FeSe-based superconductors with a hole-like band approaching the Fermi level from below; shaded crossed areas denote the energy regions around the Fermi level, where two pairing interactions operate, e.g., electron–phonon (Λ_{ph}) and spin–fluctuation (Λ_{sf}). (b) T_c and energy gap (at $T = 0$ and on different sheets of the Fermi surface) behavior during the crossing of the Fermi level by a hole-like band (the Lifshits transition). T_{c0} is the temperature of the superconducting transition in the absence of the hole-like band. All energies are given in units of Λ_{sf} [67].

Then, we can introduce $g_0 = -uv$ and the matrix of dimensionless pairing constants takes the following form:

$$\hat{g} = g_0 \begin{pmatrix} 1 & 1 & 1 & 1 \\ 1 & 1 & 1 & 1 \\ 1 & 1 & 1 & 1 \\ 1 & 1 & 1 & 1 \end{pmatrix}. \qquad (15)$$

In this case, we obtain $g_{\text{eff}} = 4g_0$, i.e., the real quadrupling of the effective pairing coupling constant, compared to the single-band model (or the model without interband pairing couplings). The generalization to the case of $n \times n$ matrices is obvious.

In Refs [66, 68], it was revealed that a certain choice of coupling constants in this model (with account for the LDA-calculated values of the partial densities of states) allows, in principle, a rather easy explanation of the observed (by ARPES) values of energy gap ratios on different pockets of the Fermi surface for a number of FeAs-based superconductors.

In Ref. [67], a similar analysis was done for a number of typical situations of electronic spectrum evolution, which can be realized in FeAs- and FeSe-based systems. It was explicitly shown that, for example, in a hole-like band approaching from below in energy (at the point Γ) and crossing the Fermi level (Lifshits transition), T_c and the values of the energy gaps on hole-like and electron-like pockets of the Fermi surface actually *grow*. In Fig. 15, we show the results of calculations [67] for a typical case which may be realized in the systems under consideration. We can see that as the distance of the hole-like band from the Fermi level E_g diminishes and changes its sign (upon the Lifshits transition) there is a significant growth of T_c and the gap values Δ_i (at $T = 0$). Specific values of parameters used in this calculations can be found in Ref. [67].

The basic conclusion from this elementary analysis is that the multiple-band structure, in general, facilitates the growth of the effective pairing coupling constant and the growth of T_c. It is also clear that the opening of new pockets on the Fermi surface (during the Lifshits transition) also leads to the growth of T_c, while closing such pockets leads to a drop in T_c. A number of experiments on FeAs systems under strong enough electron or hole doping evidently confirm these conclusions [69, 70].

At the same time, the general picture of electronic spectrum evolution during the transition from typical FeAs-based systems to intercalated FeSe systems, as well as all the data obtained for a single-layer FeSe/STO, drastically contradicts this conclusion — the high values of T_c are achieved in these systems after the disappearance of hole-like pockets around the point Γ, and only electron-like pockets remain around M points. The energy gaps appearing on these pockets are reliably measured in ARPES experiments and are practically isotropic [28, 50]. The relevant experimental data are exemplified in Fig. 16.

These data give rather convincing evidence of either d-wave pairing (case 1 above) or the usual s-wave pairing in

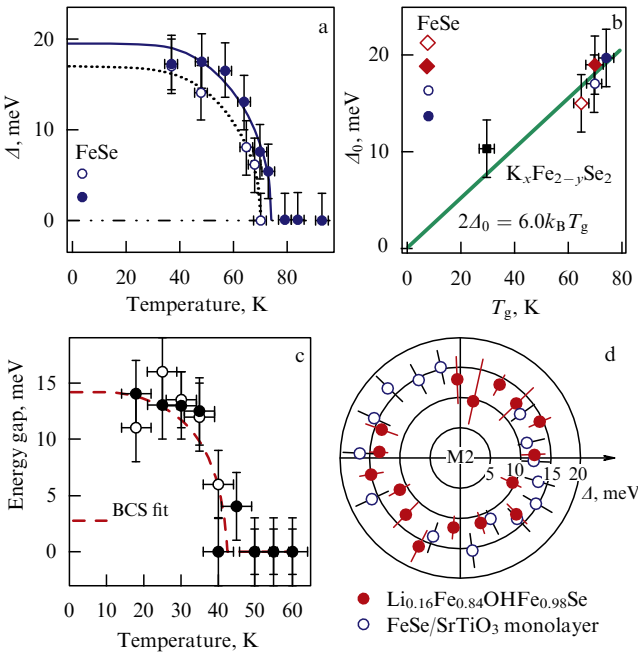

Figure 16. (a) Temperature dependence of the energy gap for two FeSe/BTO films [28]. (b) The values of the gaps for $K_xFe_{2-y}Se_2$ and FeSe monolayers [28]. (c) Temperature dependence of the energy gap in $Li_{0.16}Fe_{0.84}OHFe_{0.98}Se$ [50]. (d) Angular dependence of the energy gap in $Li_{0.16}Fe_{0.84}OHFe_{0.98}Se$ and an FeSe/STO monolayer [50].

the systems under discussion. The $s^{\pm}$ type pairing cannot be realized in these systems due to the absence (or smallness) of Fermi surface pockets around the point Γ. The absence of 'nesting' of electron-like and hole-like pockets on the Fermi surface also indicates the lacking of well-developed spin fluctuations, which can be responsible for repulsive interaction leading to a picture of $s^{\pm}$-pairing.

Apparently, the most probable scenario for these systems is s-wave pairing, when the usual isotropic gap opens on electron pockets. The variant of d-wave pairing (as in case 1) seems highly improbable. First of all, no microscopic mechanism (like spin fluctuations) has ever been proposed for realization of repulsive interaction on characteristic inverse lattice vectors connecting electron pockets at points M (or points X and Y in the Brillouin zone in Fig. 5b). This picture also contradicts direct experiments on the influence of magnetic and nonmagnetic adatoms on superconductivity in single-layer FeSe/STO films. It was reported in Ref. [71] that magnetic adatoms suppress superconductivity, while nonmagnetic adatoms barely influence it at all. This obviously corresponds to the picture of s-wave pairing.

4.3 Models of T_c enhancement in FeSe monolayer due to interaction with elementary excitations in the substrate

It is clear from the previous discussion that values of $T_c \sim 40$ K in intercalated FeSe layers can be achieved, in principle, by increasing the density of states at the Fermi level, in contrast to its value for bulk FeSe, which may be connected with the evolution of the band structure and doping effects. At the same time, it is also clear that an increase in T_c to values exceeding 65 K, observed in FeSe monolayers on STO (BTO), cannot be explained along these lines. It is natural to assume that such increase is somehow related to the nature of the STO (BTO) substrate, e.g., with additional pairing interaction of carriers in the FeSe layer appearing due to their interaction with some kind of elementary excitations in the substrate, in the spirit of the 'excitonic' mechanism, as was initially proposed by Ginzburg [1–4].

It is well known that $SrTiO_3$ is a semiconductor with an indirect energy gap of width 3.25 eV [72]. At room temperature, this compound is paraelectric with a very high dielectric constant reaching values of $\sim 10^4$ at low temperatures, remaining in the paraelectric state [73]. It is interesting to note that under electron doping in a concentration interval from 6.9×10^{18} cm^{-3} to 5.5×10^{20} cm^{-3}, $SrTiO_3$ becomes a superconductor with a maximum value of $T_c \sim 0.25$ K at an electron concentration on the order of 9×10^{19} cm^{-3} [74, 75]. The origin of superconductivity at such low concentrations (and the general shape of corresponding phase diagram) is by itself an interesting separate issue.

4.4 Excitonic mechanism by Allender, Bray, and Bardeen

The structure of FeSe films on $SrTiO_3$, shown in Fig. 3, represents the typical Ginzburg 'sandwich' [1–3], which indicates the possibility of realizing the excitonic mechanism of superconductivity. Let us consider the widely known version of this mechanism, as proposed for such a system long ago by Allender, Bray, and Bardeen (ABB) [76]. This mechanism is illustrated schematically in Fig. 17. An electron from a metal with momentum $\mathbf{k}_{1\uparrow}$ (arrow denotes spin direction) is transferred to the $\mathbf{k}_{2\uparrow}$ state due to excitation of the interband transition in a semiconductor from valence band state $\mathbf{k}_v$ to the $\mathbf{k}_c$ state in the conduction band, creating a virtual exciton. The second electron of the Cooper pair, which

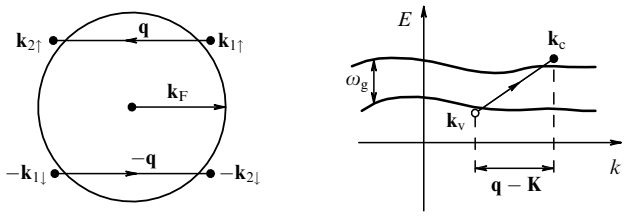

Figure 17. ABB excitonic mechanism.

resides initially in the $-\mathbf{k}_{1\downarrow}$ state, absorbs this exciton and goes into the $-\mathbf{k}_{2\downarrow}$ state. The momentum conservation law holds true: $\mathbf{q} = \mathbf{k}_2 - \mathbf{k}_1 = \mathbf{k}_v - \mathbf{k}_c + \mathbf{K}$, where $\mathbf{K}$ is an arbitrary inverse lattice vector. As a result, we obtain electron attraction within the pair, which is conceptually identical to that appearing due to phonon exchange.

In Ref. [76], a rough estimate of the corresponding attraction coupling constant was obtained as follows:

$$\lambda_{ex} = ba\mu\,\frac{\omega_p^2}{\omega_g^2}\,, \tag{16}$$

where μ is the dimensionless Coulomb potential, ω_p is the plasma frequency in a semiconductor, while ω_g is the width of the energy gap in a semiconductor, which plays the role of exciton energy. Dimensionless constant $b \sim 0.2$ defines the fraction of time the metallic electron spends inside the semiconductor, and the constant $a \sim 0.2-0.3$ is related to the screening of the Coulomb interaction within a metal. This estimate was criticized in Refs [77, 78] as an overestimate; additional arguments in favor of it were given in Ref. [79]. Without returning to this discussion, we further use the estimate given by formula (16) as obviously too optimistic.

To estimate T_c in the presence of two mechanisms of attraction (phonon and exciton), Ref. [76] proposed using the following simple expression which gives (as was shown in Ref. [76]) a better approximation to the numerical solution of the Eliashberg equations:

$$T_c = \frac{\omega_D}{1.45}\exp\left(-\frac{1}{g_{eff}}\right), \tag{17}$$

where

$$g_{eff} = \lambda_{ph}^{\star} + \frac{\lambda_{ex}^{\star} - \mu^{\star}}{1 - (\lambda_{ex}^{\star} - \mu^{\star})\,\ln(\omega_g/\omega_D)}\,, \tag{18}$$

$$\mu^{\star} = \frac{1}{1 + \mu\,\ln(E_F/\omega_g)}\,, \tag{19}$$

and the constants of electron–phonon and exciton exchange attractions are taken here in the renormalized form:

$$\lambda_{ph}^{\star} = \frac{\lambda_{ph}}{1+\lambda_{ph}}\,, \quad \lambda_{ex}^{\star} = \frac{\lambda_{ex}}{1+\lambda_{ex}}\,, \tag{20}$$

which takes into account qualitatively the effects of strong coupling, and E_F is the Fermi energy of a metallic film.

If we consider λ_{ex} a free parameter, we can easily estimate the possible extent of a T_c enhancement via the excitonic mechanism. Corresponding dependences calculated from Eqns (17)–(20) for typical values of Coulomb potential μ are

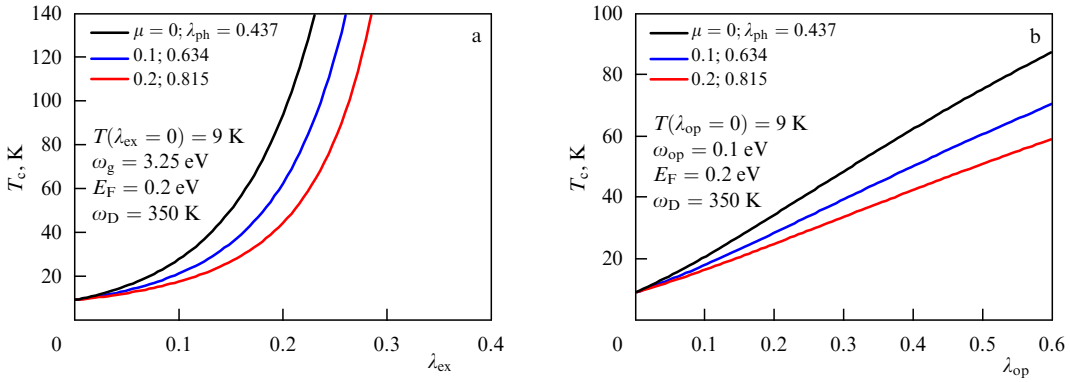

Figure 18. Dependence of T_c for FeSe/STO on the coupling constant with an ABB exciton (a) and optical phonon in STO (b).

shown in Fig. 18a. The value of ω_D was taken to be 350 K, while $\lambda_{ph} = 0.437$, as to reproduce the value of $T_c = 9$ K typical for bulk FeSe, while $E_F = 0.2$ eV was taken to be in agreement with LDA calculations of the FeSe monolayer. From Fig. 18a, we can see that for large enough values of λ_{ex} very high values of T_c can easily be obtained (as was theoretically predicted in Ref. [76]). The problem, however, is that even using the very optimistic estimate of λ_{ex} in Eqn (16), taking characteristic values of $\omega_p = 10$ eV, $\omega_g = 3.25$ eV, and for typical $\mu \sim 0.1-0.2$, we arrive at λ_{ex} values of $\sim 0.04-0.13$. Correspondingly, as we can see from Fig. 18a, even for these overoptimistic estimates, we obtain a quite modest increase in T_c and it is very far from the desirable values of $\sim 65-75$ K. These estimates convincingly demonstrate the ineffectiveness of the ABB excitonic mechanism as applied to FeSe/STO monolayers.

4.5 Interaction with optical phonons in STO

Ginzburg's initial notion to enhance T_c in 'sandwich' type structures [1–3] was based on the idea of electron interaction in metallic film with more or less high-energy excitations of an electronic nature ('excitons') within a semiconducting substrate. However, this idea can be understood in a wider context: the interaction of electrons of a metallic film with some arbitrary boson excitations in the substrate (e.g., with phonons) can lead to an increase in T_c. As we shall see, precisely this scenario is probably realized in FeSe monolayers on STO (BTO).

In $SrTiO_3$ or $BaTiO_3$ systems, almost dispersionless optical phonons exist with an unusually high excitation energy on the order of ~ 100 meV [80]. Examples of phonon dispersions and densities of states in these systems (both calculated and measured by neutron scattering method) are illustrated in Fig. 19. To estimate the prospects of T_c enhancement via interaction with such phonons, we can again utilize expressions (17)–(20) with simple replacements of $\omega_g \to \omega_{op}$ and $\lambda_{ex} \to \lambda_{op}$, where ω_{op} is the characteristic frequency of an optical phonon, and λ_{op} is the dimensionless coupling constant for such a phonon with electrons in a metallic film. Results of such calculations of T_c versus λ_{op} (similar to those shown in Fig. 18a for the ABB excitonic mechanism) with the choice of $\omega_{op} = 0.1$ eV are represented

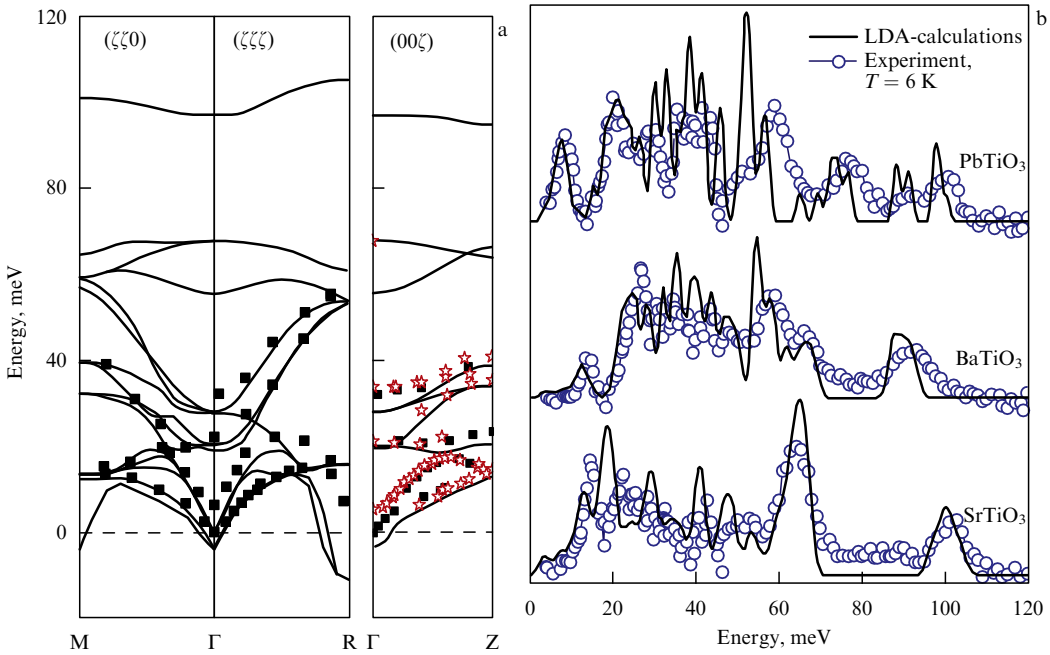

Figure 19. Phonons in $SrTiO_3$ and similar compounds: (a) phonon dispersions in $SrTiO_3$, both calculated and measured by inelastic neutron scattering, and (b) phonon density of states in $PbTiO_3$, $BaTiO_3$, and $SrTiO_3$ from neutron scattering and calculations [80].

in Fig. 18b. It can be seen that for large enough values of $\lambda_{op} \sim 0.5-0.6$ and not very large μ we can easily achieve values of $T_c \sim 60-80$ K, corresponding to experiments on FeSe/STO (BTO), even if we start from a relatively low initial T_c of about 9 K for FeSe in the absence of additional pairing interaction. Corresponding values of λ_{op} seem to be realistic enough, and below we shall present concrete evidence that interaction with optical phonons in these structures can be strong enough.

The idea that interactions with optical phonons from STO can play a significant role in the physics of FeSe/STO monolayers was first proposed by Lee et al. [49] in connection with ARPES measurements done in this work, which demonstrated the formation of a 'shadow' band at point M in the Brillouin zone, as shown in Fig. 11b. This band is situated approximately 100 meV below the main conduction electron band and practically replicates its dispersion. The formation of such a band can be linked to the interaction of FeSe electrons with an optical phonon of the corresponding energy from STO. To understand this situation, we have to consider a realistic enough picture of FeSe monolayer electrons interacting with optical phonons of STO, which was proposed in Ref. [49] and will be briefly described below (cf. also Ref. [81]).

Since STO resides in an almost ferroelectric state, it is natural to expect that charge transfer at the interface can induce the appearance of a layer of ordered dipoles. Free carriers in STO, appearing, for example, due to oxygen vacancies (or Nb doping), will screen the electric field far from the interface. Then, the dipole layer will be localized close to the interface. The appearance of dipoles is connected with the displacement of Ti cations relative to oxygen anions, so that oscillations of these anions will lead to modulation of the dipole potential along the FeSe layer. This situation is shown schematically in Fig. 20a.

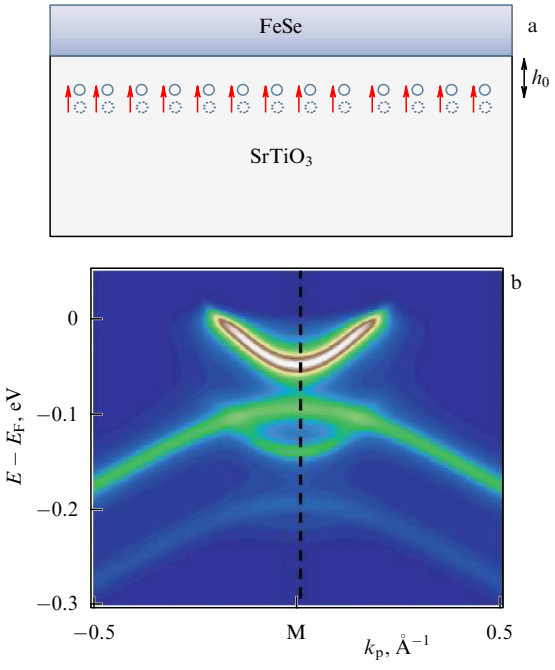

Figure 20. (Color online.) (a) Diagrams of dipole excitations close to an FeSe/STO interface. (b) Calculated electron spectral density in FeSe/STO in the model with a dominant forward scattering [49].

Let δP_z denote the change in dipole moment due to displacement of oxygen anions in the direction perpendicular to the interface:

$$\delta P_z(x, y, -h_0) = q_{\text{eff}}\, \delta h(x, y, -h_0)\,. \tag{21}$$

Here, x, y are coordinates in the plane parallel to the interface, the origin of the z-axis is chosen in the Fe plane, and q_{eff} is the dipole charge. With respect to the Fe plane, the dipole layer is at $z = -h_0$. The induced change in the dipole potential in the Fe plane, connected with the 'frozen' displacement of oxygens, is given by the following expression:

$$\Phi(x, y, 0) = \frac{\epsilon_{\|}^{1/2} q_{\text{eff}} h_0 n_d}{\epsilon_{\perp}^{3/2}} \int \mathrm{d}x'\, \mathrm{d}y' \times \frac{\delta h(x', y', -h_0)}{\left[(\epsilon_{\|}/\epsilon_{\perp})\, h_0^2 + (x - x')^2 + (y - y')^2\right]^{3/2}}\,. \tag{22}$$

Performing the Fourier transform over x, y, we get

$$\Phi(\mathbf{q}_{\|}, 0) = \frac{2\pi q_{\text{eff}} n_d}{\epsilon_{\perp}} \exp\left(-|\mathbf{q}_{\|}| h_0 \sqrt{\frac{\epsilon_{\|}}{\epsilon_{\perp}}}\right) \delta h(\mathbf{q}_{\|}, -h_0)\,. \tag{23}$$

Here, $\mathbf{q}_{\|}$ is the wave vector parallel to the interface, $\epsilon_{\|}$, $\epsilon_{\perp}$ are dielectric constants parallel and perpendicular to the interface, and n_d is the density of the dipoles per unit area of the interface. Because electrons in FeSe move parallel to the interface, they contribute only to $\epsilon_{\|}$. As to carriers in STO, besides their role in screening, which we have mentioned above, they make approximately equal contributions (STO possesses a cubic structure) to both $\epsilon_{\|}$ and $\epsilon_{\perp}$. Thus, we can expect that the total dielectric constant $\epsilon_{\|}$ is much greater than $\epsilon_{\perp}$.

From Eqn (23), it becomes clear that the value of the matrix element of electron–phonon interaction has an important dependence on $\mathbf{q}_{\|}$, so that it can be written out as

$$\Gamma(p_{\|}, \mathbf{q}_{\|}) = \frac{2\pi q_{\text{eff}} n_d}{\epsilon_{\perp}} \exp\left(-\frac{|\mathbf{q}_{\|}|}{q_0}\right), \tag{24}$$

$$q_0^{-1} = h_0 \sqrt{\frac{\epsilon_{\|}}{\epsilon_{\perp}}}\,. \tag{25}$$

The fact that $\epsilon_{\|} \gg \epsilon_{\perp}$ leads to q_0 suppression by a factor of $1/\sqrt{\epsilon_{\|}/\epsilon_{\perp}}$ which, in turn, leads to a fairly sharp peak in electron–phonon interaction at $\mathbf{q}_{\|} = 0$.

Such a dominating role of forward scattering explains the appearance of the 'shadow' band in the electronic spectrum, which replicates the dispersion of the main band. In the case of electron–phonon interaction acting in the wide range of transferred momenta, it will lead to a superposition of many bands, each being moved by its own scattering vector, which will lead to a general smearing of the 'shadow' band.

The standard numerical calculation of second–order electron self-energy due to electron–phonon interaction was performed in Ref. [49] with the coupling constant written as $g(\mathbf{q}) = g_0 \exp(-|\mathbf{q}|/q_0)$, with $g_0 = 0.04$ eV, $q_0 = 0.3/a$ ($a = 3.9$ Å), optical phonon frequency $\Omega_0 = 80$ meV, and the bare spectrum of electrons and holes (one-dimensional — along the $\Gamma-\mathrm{M}$ direction) written as $\epsilon_{e,h}(k) = -2t_{e,h}\cos(k/a) - \mu_{e,h}$ (close to the point M) with $t_e = 125$ meV, $t_h = 30$ meV, $\mu_e = -185$ meV, and $\mu_h = 175$ meV, where all numerical parameters were taken from fitting the ARPES experiment data. Results of such a calculation for electron spectral density (imaginary part of Green's function)

are plotted in Fig. 20b. We can see that these calculations are in excellent agreement with the ARPES data in Fig. 11b. The standard dimensionless electron–phonon coupling constant can be estimated numerically using the same values of all the parameters, yielding [49]

$$\lambda = \frac{2}{N\Omega_0}\frac{\sum_{\mathbf{k},\mathbf{q}} \left|g(\mathbf{q})\right|^2 \delta\left(\epsilon_{\mathrm{e}}(\mathbf{k})\right) \delta(\epsilon_{\mathrm{e}}(\mathbf{k}-\mathbf{q}))}{\sum_{\mathbf{k}} \delta\left(\epsilon_{\mathrm{e}}(\mathbf{k})\right)} = 0.5\,, \qquad (26)$$

(N is the number of lattice sites), which is (as noted above) quite sufficient for a significant increase in T_{c} in the FeSe/STO monolayer. As we shall see below, the peculiarities of the model of electron–phonon interaction with a dominant forward scattering also lead to some other, even more important, effects favorable to the enhancement of T_{c}.

4.6 Cooper pairing in the model with a dominant forward scattering

Dominant forward scattering in electron–phonon interactions was for a long time considered a special cause of T_{c} enhancement due to the specific dependences differing from the standard BCS, which appear in this model [82, 83]. These papers analyzed the possible role of such interactions in cuprates. An application of these ideas to FeSe/STO was considered recently in Refs [84, 85].

In the weak coupling approximation for the case of s-wave pairing, the gap equation in Eliashberg theory reduces to the following

$$\Delta(\mathrm{i}\varepsilon_n) = -\frac{T}{N}\sum_{\mathbf{q},m} \left|g(\mathbf{q})\right|^2 D(\mathbf{q}, \mathrm{i}\varepsilon_n - \mathrm{i}\varepsilon_m) \times \frac{\Delta(\mathrm{i}\varepsilon_m)}{(\varepsilon_m)^2 + \xi^2_{\mathbf{k}+\mathbf{q}} + \Delta^2(\mathrm{i}\varepsilon_m)}\,, \qquad (27)$$

where $D(\mathbf{q}, \mathrm{i}\varepsilon_n - \mathrm{i}\varepsilon_m) = -2\Omega_{\mathbf{q}}/[(\varepsilon_n - \varepsilon_m)^2 + \Omega^2_{\mathbf{q}}]$ is the Matsubara Green's function of an optical phonon with frequency $\Omega_{\mathbf{q}}$, $\xi_{\mathbf{k}} = v_{\mathrm{F}}(|\mathbf{k}| - p_{\mathrm{F}})$ is the electronic spectrum close to the Fermi level (v_{F}, p_{F} are Fermi velocity and momentum), and $\varepsilon_n = (2n+1)\,\pi T$ is the fermion Matsubara frequency.

Before going to the results of the numerical solution to equation (27), let us consider the elementary model of exactly forward scattering by phonons, when all calculations can be done analytically. For this purpose, we introduce $|g(\mathbf{q})|^2 = g_0^2 N\delta_{\mathbf{q}} = (2\pi)^2\delta(\mathbf{q})$. Then, gap equation (27) on the Fermi surface is easily transformed to

$$\Delta(\mathrm{i}\varepsilon_n) = \lambda_{\mathrm{m}}\Omega_0^2 T_{\mathrm{c}} \sum_m \frac{\Delta(\mathrm{i}\varepsilon_m)}{\varepsilon_m^2 + \Delta^2(\mathrm{i}\varepsilon_m)} \frac{2\Omega_0}{\Omega_0^2 + (\varepsilon_n - \varepsilon_m)^2}\,, \qquad (28)$$

where we have introduced the dimensionless coupling constant

$$\lambda_{\mathrm{m}} = \frac{g_0^2}{\Omega_0^2}\,. \qquad (29)$$

Notice that this definition is somehow different from the standard definition of the electron–phonon coupling constant (26).

To find the critical temperature T_{c}, the authors of Ref. [84] used the following *Ansatz* for the energy gap function:

$$\Delta(\mathrm{i}\varepsilon_n) = \frac{\Delta_0}{1 + (\varepsilon_n/\Omega_0)^2}\,. \qquad (30)$$

Then, linearizing the gap equation, we arrive at the following equation for T_{c} [84]:

$$1 = \lambda_{\mathrm{m}}\Omega_0^2 T_{\mathrm{c}} \sum_m \frac{2\Omega_0}{\varepsilon_m^2(1 + \varepsilon_m^2/\Omega_0^2)(\Omega_0^2 + \varepsilon_m^2)}\,. \qquad (31)$$

The sum over Matsubara frequencies is calculated directly, and we obtain

$$1 = \frac{\lambda_{\mathrm{m}}}{2T_{\mathrm{c}}} \frac{2\Omega_0 + \Omega_0 \cosh(\Omega_0/T_{\mathrm{c}}) - 3T_{\mathrm{c}}\sinh(\Omega_0/T_{\mathrm{c}})}{1 + \cosh(\Omega_0/T_{\mathrm{c}})}\,. \qquad (32)$$

Since for FeSe/STO one has $T_{\mathrm{c}} \ll \Omega_0$, we can use here the asymptotic form of hyperbolic functions, and in the leading approximation the critical temperature becomes the quasilinear function of the coupling constant (for its small values):

$$T_{\mathrm{c}} = \frac{\lambda_{\mathrm{m}}}{2 + 3\lambda_{\mathrm{m}}}\,\Omega_0\,. \qquad (33)$$

A similar result was previously obtained in the context of cuprate physics [82, 83]. For $\lambda_{\mathrm{m}} = 0.16$ and $\Omega_0 = 100$ meV, we get $T_{\mathrm{c}} = 75$ K, which is rather unexpected for such a small value of λ_{m}.

This value of T_{c} can be compared with the standard expression of BCS theory, where the linearized equation for T_{c} takes the following form:

$$1 = \pi T_{\mathrm{c}}\lambda_{\mathrm{m}} \sum_{|\varepsilon_m| < \omega_{\mathrm{D}}} \frac{1}{|\varepsilon_m|} = \lambda_{\mathrm{m}}\left[\ln\left(\frac{\omega_{\mathrm{D}}}{2\pi T_{\mathrm{c}}}\right) - \psi\left(\frac{1}{2}\right)\right], \qquad (34)$$

where we have used the asymptotic form at large $\omega_{\mathrm{D}}/T_{\mathrm{c}}$. This leads to the usual BCS expression: $T_{\mathrm{c}} = 1.13\omega_{\mathrm{D}}\exp(-1/\lambda_{\mathrm{m}})$, so that for $\lambda_{\mathrm{m}} = 0.16$ and $\omega_{\mathrm{D}} = 100$ meV we obtain $T_{\mathrm{c}} = 2.5$ K.

Comparing these results for T_{c}, we can conclude that the significant T_{c} enhancement obtained above appears due to the effective exclusion of momentum integration in the Eliashberg equation, which is related to the strong interaction peak at $\mathbf{q} = 0$. In the BCS model, we integrate over the whole Fermi surface and all momenta enter with the same weight, which leads to the appearance of the $\sum_m 1/|\varepsilon_m|$ term in the equation for T_{c} and to the corresponding logarithmic behavior. In the case of forward scattering, integration over momenta is lifted, so that only the ε_m^{-2} term remains in the sum over frequencies, which leads to a $1/T_{\mathrm{c}}$ type behavior. Due to this, the model with strong forward scattering leads to the effective mechanism of T_{c} enhancement [82, 83].

Let us now discuss the numerical results for the general case [84]. In a realistic situation, the forward scattering dominates in the finite region of momentum space, with the size determined by the parameter q_0. The numerical solution of the Eliashberg equations with the coupling constant of the form $g(\mathbf{q}) = g_0\exp(-|\mathbf{q}|/q_0)$ gives the temperature behavior of the superconducting gap (at the lowest Matsubara frequency) $\Delta(\mathrm{i}\pi T)$ shown in Fig. 21 (for several values of λ_{m} and $q_0 = 0.1/a$). We can see that T_{c} is already high enough for modest enough values of λ_{m} and grows approximately linearly in λ_{m}, as long as we remain in the weak coupling region. The finiteness of q_0 leads to some suppression of T_{c}, unlike the case of exact forward scattering (cf. the insert to Fig. 21), but in general the quasilinear dependence of T_{c} on λ_{m} can guarantee the values of T_{c} observed in FeSe/STO films.

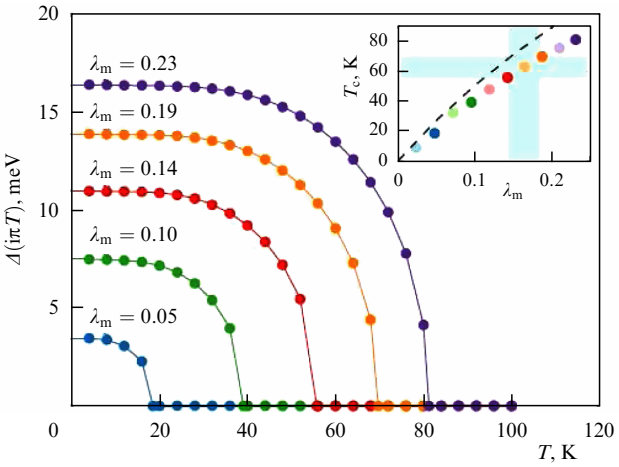

Figure 21. Temperature dependence of the energy gap $\Delta(i\pi T)$ (at the smallest Matsubara frequency) in the model with a dominant forward scattering ($q_0 = 0.1/a$) for different values of the coupling constant. In the inset, the dashed line shows the T_c-dependence of the coupling constant in the case of exactly forward scattering (33), while the dots represent the results of numerical calculations [84]. The shaded region covers the interval of λ_m values appropriate for FeSe/STO.

In the framework of this model, it is rather easy to explain the formation of the 'shadow' band in the vicinity of the M point [84, 85].

4.7 Nonadiabatic superconductivity and other problems

We have already noted above that the characteristic feature of the electronic spectrum of superconductors containing FeSe monolayers is the formation of an unusually 'shallow' electronic band in the vicinity of point M in the Brillouin zone (cf. Figs 9d, 11b). The value of Fermi energy $E_F \sim 0.05$ eV in these systems is almost an order of magnitude less than the values obtained in LDA and LDA + DMFT calculations. Such a small value of E_F creates additional difficulties for a consistent theory of superconductivity in the FeSe/STO system. Gor'kov [86] was the first to note that we are dealing here with an unusual situation, when the energy ~ 100 meV of an optical phonon in STO is significantly higher than the Fermi energy equal to ~ 50 meV.

Let us recall that in the great majority of superconductors we have the opposite inequality, $\omega_D \ll E_F$, which allows us to use the adiabatic approximation in describing the effects of electron–phonon interaction, which is based on the inequality $\omega_D/E_F \sim (m/M)^{1/2} \ll 1$ (m is the electron mass, and M is an ion mass). Then (as in the normal state), we can apply the Migdal theorem and ignore all vertex corrections to electron–phonon interactions, limiting ourselves to second-order diagrams for electron self-energy. In particular, the standard derivation of Eliashberg equations is entirely based on the adiabatic approximation, so that the common term is the Migdal–Eliashberg theory.

Breaking the relevant inequality in the FeSe/STO system means that the theory explaining T_c enhancement is to be developed, from the very beginning, but in the *antiadiabatic* approximation. An attempt to build such a theory was undertaken in recent papers by Gor'kov [86–88]. In particular, Refs [86, 87] were devoted to the FeSe/STO system and the general aspects of the problem, while a new theory was proposed in Ref. [88] for describing superconductivity in doped $SrTiO_3$, which, as was noted above, is by itself quite an unusual superconductor [74, 75].

Obviously, the frame of our review does not allow us to delve deeply into the discussion of rather complicated theoretical problems, so that we shall limit ourselves only to a qualitative presentation of the results obtained in Refs [86, 87], which are directly relevant to superconductivity in FeSe/STO. The only approximation which can apparently be used here is a *weak coupling* approximation, when the smallness of the electron–phonon coupling constant by itself allows neglecting of vertex corrections and the usual (ladder) series of Feynman diagrams in the Cooper channel to be summed. It is natural that in antiadiabatic approximation the cut-off of logarithmic divergence in the Cooper channel takes place not at phonon frequencies, but at energies on the order of the Fermi energy E_F (or the bandwidth) [87], so we can expect that $T_c \sim E_F \exp(-1/\lambda)$, where λ is determined by the details of the pairing interaction.

The interaction of FeSe electrons with longitudinal surface phonons at the STO interface can be introduced [86] via interactions with the polarization induced by these phonons:

$$\mathbf{P} = F_C \mathbf{u}\,, \tag{35}$$

where $\mathbf{u}$ is the atomic displacement, and coefficient F_C is defined by the model of electron interaction with surface longitudinal optical (SLO) phonons on the surface of an insulator [89]:

$$F_{C,i} = \left[4\pi e^2\,\frac{\omega^i_{SLO}}{2}\left(\frac{1}{\epsilon_\infty + 1} - \frac{1}{\epsilon_0}\right)\right]^{1/2}, \tag{36}$$

where the subscript or superscript i enumerates phonon branches, ϵ_0 and ϵ_∞ are static and optical dielectric constants of the bulk insulator, and ω^i_{SLO} is the frequency of the ith SLO phonon.

The matrix element for two-electron scattering due to the exchange of a surface phonon then takes the form

$$M_i(\mathbf{q}, \varepsilon_n - \varepsilon_m) = -\frac{4\pi e^2}{|\mathbf{q}|}\left(\frac{1}{\epsilon_\infty + 1} - \frac{1}{\epsilon_0}\right) D^i_{SLO}(\mathbf{q}, \varepsilon_n - \varepsilon_m)\,, \tag{37}$$

where $D^i_{SLO}(\mathbf{q})$ is Green's function of the STO phonon, namely

$$D^i_{SLO}(\mathbf{q}, \varepsilon_n - \varepsilon_m) = \frac{(\omega^i_{SLO})^2}{(\omega^i_{SLO})^2 + (\varepsilon_n - \varepsilon_m)^2}\,, \tag{38}$$

where $\mathbf{q} = \mathbf{p} - \mathbf{k}$ and $\varepsilon_n - \varepsilon_m$ are the momentum and (Matsubara) frequency exchanged between electrons.

In a bulk insulator, the well-known Lyddane–Sachs–Teller relation holds between the frequencies of longitudinal (LO) and transverse (TO) optical phonons: $\omega^2_{LO}/\omega^2_{TO} = \epsilon_0/\epsilon_\infty$. According to Ref. [89], the frequency of the longitudinal surface phonon is given by the following expression: $\omega^2_{SLO}/\omega^2_{TO} = \epsilon_0 + 1/\epsilon_\infty + 1$. It should be stressed that the values of ϵ_0 and ϵ_∞ are considered here as model parameters depending on the details of STO surface preparation in the process of creating the FeSe/STO structures (e.g., $SrTiO_3$ doping by Nb) [86].

Finally, for the matrix element of two-electron scattering due to the exchange of surface LO phonons and (two-dimensional) Coulomb repulsion, dropping some factors

that are irrelevant at the moment [86], we obtain the following expression

$$M_{\rm tot}(\mathbf{p},\varepsilon_n|\mathbf{k},\varepsilon_m)=\frac{4\pi e^2}{(\epsilon_\infty+1)\,q}-\sum_i\frac{4\pi e^2}{(\epsilon_\infty+1)\,q}\,D^i_{\rm SLO}(\varepsilon_n-\varepsilon_m)\,. \quad (39)$$

Here, the summation is performed over three IR-active phonons at point Γ of the bulk $SrTiO_3$, whose frequencies satisfy the inequality $\omega^i_{\rm LO}>T_{\rm c}$ [80]. In fact, in $SrTiO_3$ we have a single LO mode which has a very large gap compared to the frequencies of all TO phonons, and which is of fundamental importance here compensating for the Coulomb repulsion in Eqn (39) for $|\varepsilon_n-\varepsilon_m|\ll\omega_{\rm LO}$. The remaining LO phonons, as usual, make an additional contribution to attraction. Since the inequality $\epsilon_0\gg\epsilon_\infty$ holds in $SrTiO_3$, we have left in Eqn (39) only the contributions from terms with $\epsilon_\infty+1$.

In the extreme antiadiabatic limit, when $\omega_{\rm SLO}\gg E_{\rm F}$, we can ignore $(\varepsilon_n-\varepsilon_m)^2$ terms in the denominator of the phonon Green's function, so that the matrix element of two-electron interaction can be written out as

$$M_{\rm tot}(\mathbf{p},\varepsilon_n|\mathbf{k},\varepsilon_m)=M(\mathbf{p}-\mathbf{k})\approx-2\alpha^2\,\frac{4\pi e^2}{|\mathbf{p}-\mathbf{k}|(\epsilon_\infty+1)}<0\,. \quad (40)$$

Here, $\alpha^2<1$ represents some numerical correction factor [86].

Now, we also have to take into account the screening of Coulomb interaction by the two-dimensional electron gas of FeSe. Then, in the random phase approximation (RPA) we get [86]

$$M_{\rm scr}(\mathbf{p}-\mathbf{k})\approx-2\alpha^2\,\frac{4\pi e^2}{\epsilon_\infty}\,\frac{1}{|\mathbf{p}-\mathbf{k}|+4e^2m/(\epsilon_\infty+1)}\,. \quad (41)$$

In an experimental situation typical for FeSe/STO, the inverse screening length q_0 is small compared with Fermi momentum $p_{\rm F}$, so that the following inequality always holds:

$$\frac{p_{\rm F}}{q_0}=\frac{p_{\rm F}(\epsilon_\infty+1)}{e^2m}\gg1\,. \quad (42)$$

Introducing the effective Bohr radius $a_{\rm B}=(\epsilon_\infty+1)/(e^2m)$, this inequality can be rewritten as $p_{\rm F}a_{\rm B}\gg1$.

In the weak coupling approximation, the linearized gap equation can be written out as [86]

$$\Delta(\mathbf{p})=-T\sum_m\int\frac{{\rm d}^2k}{(2\pi)^2}\,M_{\rm scr}(\mathbf{p}-\mathbf{k})\,G(-\mathbf{k})\,G(\mathbf{k})\,\Delta(\mathbf{k})\,, \quad (43)$$

where the product of two Green's functions is $G(-\mathbf{k})\,G(\mathbf{k})=[\varepsilon_m^2+\xi_{\mathbf{k}}^2]^{-1}$.

Then, after somewhat cumbersome, though direct, analysis, we can obtain the following result for the critical temperature $T_{\rm c}$:

$$T_{\rm c}(x)\sim\frac{p_{\rm F}^2}{2m}\exp\left(-\frac{1}{\alpha^2\lambda(x)}\right)=\frac{2}{ma_{\rm B}^2}\,x^2\exp\left(-\frac{1}{\alpha^2\lambda(x)}\right), \quad (44)$$

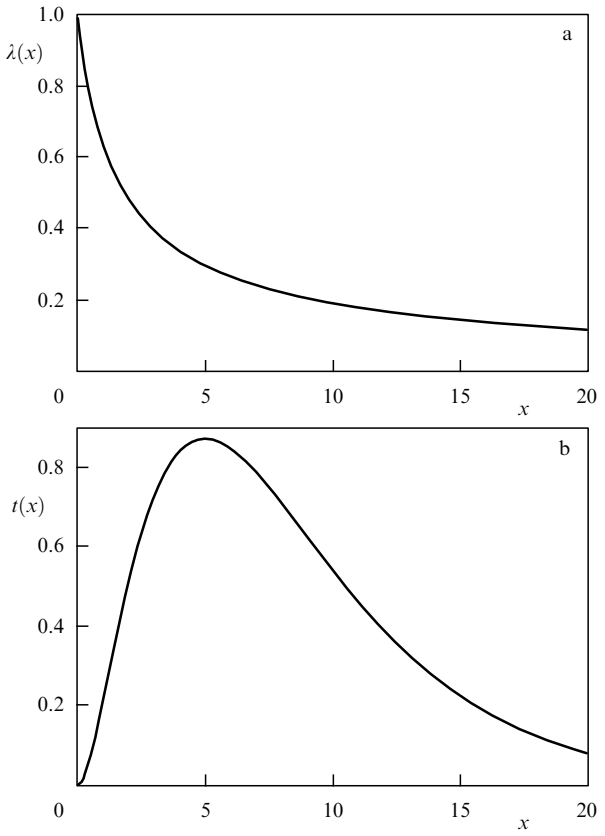

Figure 22. Dimensionless functions determining $T_{\rm c}$ in Gor'kov's model: (a) $\lambda(x)$ function, (b) $t(x)=x^2\exp(-1/\lambda(x))$ function.

where we have introduced the dimensionless parameter $x=(p_{\rm F}a_{\rm B})/2$, and

$$\lambda(x)=\frac{2}{\pi}\int_0^{\pi/2}\frac{{\rm d}u}{x\sin u+1}\,. \quad (45)$$

For our estimates, we can just put $\alpha^2=1$. Two dimensionless functions $\lambda(x)$ and $t(x)=x^2\exp(-1/\lambda(x))$ are plotted in Fig. 22. The maximum in $t(x)$ appears due to two competing factors: at a given value of $a_{\rm B}$, the critical temperature first grows with increasing electron concentration and then the increased screening suppresses the effective coupling constant.

Direct calculations [86] show that this model also reproduces the 'shadow' band in the electronic spectrum in the vicinity of point M. This is essentially due to the fact that from the form of pairing interaction (41) it becomes clear that Gor'kov's model also produces significant growth of interaction at small transferred momenta. The effective interaction is concentrated in the momentum region inside the inverse screening length q_0 satisfying inequality (42), so that $q_0\ll1/a$, in accordance with the estimates given above for the model with a dominant forward scattering.

Let us make the simplest estimate of the maximum value of $T_{\rm c}$ which can be achieved in this model. We put $E_{\rm F}=60$ meV, which approximately corresponds to ARPES experiments. The maximum of $t(x)$, as can be seen from Fig. 22b, is close to $x=5$, which corresponds to $\lambda(5)=0.3$ (cf. Fig. 22a). Then it follows that $T_{\rm c}\approx0.03\times60$ meV ≈20 K. Thus, this mechanism by itself cannot explain the values of $T_{\rm c}>60$ K, observed in experiments on FeSe/STO.

However, in combination with some additional pairing interaction mechanism responsible for the initial value of $T_c \sim 8$ K in bulk FeSe (either due to the usual electron–phonon pairing mechanism or pairing due to exchange of antiferromagnetic fluctuations), we can obtain significantly higher values of T_c [86]. For example, if for the spin-fluctuation mechanism we make use of the estimate $T_c \sim E_F \exp(-1/\lambda_{sf})$, then at $E_F = 60$ meV the initial value of T_c is obtained for $\lambda_{sf} = 0.23$. Then, the combined pairing constant $\lambda = \lambda_{sf} + \lambda(5) = 0.48$ (assuming the same cut-off in the Cooper channel, the coupling constants are simply summed), leading to $T_c \approx 0.15 \times 60$ meV ≈ 90 K. In the case of combination with the conventional electron–phonon mechanism, we can estimate T_c using the upper curve (corresponding to $\mu = 0$) in Fig. 18b. Then, taking $\lambda_{op} = \lambda(5) = 0.3$, we immediately arrive at $T_c \approx 50$ K.

The situation with nonadiabatic effects in the model with a dominant forward scattering has recently been analyzed in Ref. [86] by direct calculations of vertex corrections to the electron–phonon interaction with the coupling constant $|g(\mathbf{q})|^2 = g_0^2 N \delta_{\mathbf{q}}$. It turned out that in this model the Migdal theorem breaks down for any values of the ratio Ω_0/E_F, which does not appear at all in vertex corrections. However, vertex corrections remain small for small values of the parameter $\lambda_m = g_0^2/\Omega_0^2$, and we have seen above that to explain the current experiments on FeSe/STO it is sufficient to keep the values of $\lambda_m \sim 0.15-0.20$.

The small values of Fermi energy E_F in the electron band at point M observed in intercalated FeSe systems and FeSe/STO (BTO) lead to one more important consequence. Typical values of the superconducting gap at low temperatures, observed in ARPES measurements on these systems, are $\Delta \sim 15-20$ meV (cf. Fig. 16). Correspondingly, here we have unusually large ratios $\Delta/E_F \sim 0.25-0.3$, which unambiguously points to the fact that these systems belong to the region of BCS–Bose crossover [90, 91], when the size of Cooper pairs, determined by coherence length ξ, becomes small and approaches the interelectron spacing, when $p_F \xi \sim \xi/a \sim 1$. The picture of superconducting transition and all estimates for physical characteristics like T_c in this region are different from those for the weak-coupling BCS theory and are closer to the picture of Bose–Einstein condensation of compact Cooper pairs [90, 91].

The emergence of such a situation was earlier noted in connection with some experiments on the $FeSe_xTe_{1-x}$ system [92], and also for bulk FeSe in an external magnetic field [93].

From the theoretical standpoint, we need here a special treatment [90, 91]. Unfortunately, a theoretical description of the BCS–Bose crossover for multiple-band systems like FeSe has remained, up to now, almost undeveloped. We can quote only the recent paper [94], but detailed discussion of different possibilities appearing here is outside the scope of the current review.

5. Conclusions

Basic conclusions from our discussion can be formulated as follows. A number of aspects of the physics of the systems under investigation are more or less clear:

• The electronic spectrum of intercalated FeSe systems and FeSe/STO (BTO) is significantly different from the spectrum of FeAs-based systems and bulk FeSe. Here, we have only electron-like Fermi surfaces surrounding the M points in the Brillouin zone. Hole-like Fermi surfaces 'sink' under the Fermi level. There are no 'nesting' properties of Fermi surfaces at all;

• The values of superconducting critical temperature T_c in intercalated systems are well correlated with the value of the total density of states at the Fermi level, obtained by LDA calculations, independently of the microscopic nature of pairing;

• Cooper pairing most probably reduces to the usual s-wave pairing; there is no possibility of $s^{\pm}$-pairing because of the absence of hole-like Fermi surfaces, while d-wave pairing also seems highly improbable;

• The record values of T_c observed in FeSe monolayers on STO (BTO) are apparently related to the additional pairing mechanism emerging, due to interaction with high-energy optical phonons of STO (BTO) in the geometry of the Ginzburg 'sandwich'. In this case, we may speak here of the realization of a 'pseudoexcitonic' pairing mechanism.

At the same time, many questions remain to be resolved:

• To date, the observation of the values of $T_c \sim 100$ K, reported in Ref. [25], has remained unconfirmed;

• The origin of unusually 'shallow' electron bands with extremely small values of the Fermi energy in the vicinity of M points remains unclear. This is probably related to our poor understanding of the role of electron correlations;

• The data on possible magnetically ordered phases in intercalated FeSe-based systems remain rather indeterminate. Practically nothing is known about the possible types of magnetic ordering in FeSe/STO (BTO) films;

• From the theoretical point of view, it remains obscure why the disappearance of some Fermi surfaces in FeSe systems is followed by a significant *increase* in T_c, contradicting general expectations based on the multiple-band BCS model;

• Practically no serious theoretical developments are known concerning possible manifestations of BCS–Bose crossover effects in these systems, their experimental consequences, or the role of these effects in the formation of high values of T_c.

Finally, let us discuss several proposals for possible ways to further increase T_c in FeSe monolayers on STO (or BTO). If we accept the concept of the decisive role of interactions with elementary excitations in the substrate (most probably with optical phonons), the natural idea appears of creating multiple-layer films and superstructures, like those demonstrated in Fig. 23 [81]. In particular, the structure shown in Fig. 23a is the direct realization of the Ginzburg 'sandwich', precisely as was proposed in his original work [1–3]. It seems

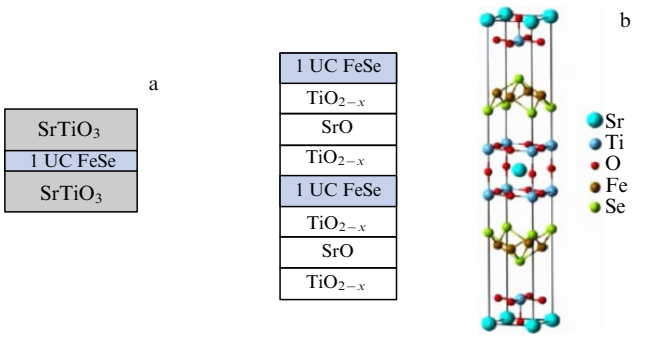

Figure 23. Possible FeSe/STO-based superstructures, where an increase in T_c can be expected [81]: (a) Ginzburg's 'sandwich' with two STO layers, and (b) multiple-layer superstructure.

obvious that the presence of the second $SrTiO_3$ layer (or the similar $BaTiO_3$ layer) will lead to the effective enhancement of the pairing constant due to interaction with optical phonons in the second STO layer. Obviously, the presence of the second STO layer will also serve as a good protection of the conductive FeSe layer from the external environment. Similarly, attempts to create bulk superstructures (compounds), like those shown in Fig. 23b, seem to be very promising. Despite all the technical problems appearing on the path to creating such structures (or their analogues), this way seems to have great potential. There is no doubt that the last word on studies of high-temperature superconductivity in FeSe-based monolayers and other similar systems is yet to be heard.

The author is grateful to E Z Kuchinskii and I A Nekrasov for discussions on a number of problems dealt with in this review, as well as for their help with some numerical computations.

This research was supported by the Russian Science Foundation grant No. 14-12-00502. Calculations of the electronic spectra of FeSe systems and the comparative analysis of mechanisms of Cooper pairing were performed under FASO State contract No. 0389-2014-0001 with a partial support from RFBR grant No. 14-02-00065.

Notes added in proof

During the time after the submission of this review, a number of new experimental and theoretical studies dealing with the systems under discussion have appeared in the literature. Below, we cite some of them with brief comments.

In Ref. [95], single-layer FeSe films on STO were studied at different doping levels, which were achieved by surface deposition of potassium *in situ*. A sharp growth of T_c from 60 K to 75 K was observed, accompanied by a Lifshits transition with the formation of a small *electron-like* pocket of the Fermi surface around point Γ, which was confirmed by ARPES measurements. Notice that such T_c behavior is in complete accordance with qualitative conclusions of the multiple-band superconductivity theory, discussed in our review.

Important results were achieved in Ref. [96], where high values of $T_c \sim 65$ K were obtained for FeSe monolayers on the (100) plane of rutile TiO_2. These results give evidence that the ferroelectric properties of $SrTiO_3$ (absent for TiO_2) are irrelevant for T_c growth in the systems under discussion and almost unambiguously confirm the important role of interactions with longitudinal optical phonons in the substrate, which in TiO_2 are practically the same as in STO. The electronic spectrum of FeSe films on TiO_2 measured by ARPES was observed to be practically the same as in FeSe/STO, with a 'replica' band clearly observed approximately 100 meV below the electron band at point M, similar to that observed in FeSe/STO [49].

Experiments carried out in Ref. [97] and taking advantage of high-resolution electron energy loss spectroscopy (HREELS) confirmed the presence of strong electron–phonon interaction at the FeSe/STO interface, giving an experimental estimate of the coupling constant with a 92-meV optical phonon in STO of ~ 1.

Theoretical results of Refs [49, 81, 84, 85] were critically reconsidered in Ref. [98]. However, the qualitative conclusion about the important role of a dominant forward scattering of electrons in the FeSe monolayer by the optical phonons of $SrTiO_3$ for an increase in T_c in FeSe/STO was essentially confirmed.

In Ref. [99], the '*first principles*' calculations of electron–phonon coupling in the FeSe/STO system were performed, confirming the significant enhancement of this interaction in the region of small transferred momenta. However, the numerical values of the corresponding coupling constant were too low to explain the experimentally observed high values of T_c. At the same time, it should be noted that calculations of the electronic spectrum for the FeSe/STO system done in this study were made neglecting the possible role of electron correlations, and spectra obtained were quite different from those observed in ARPES experiments (absence of the 'shallow' band). Thus, the conclusions about the value of the coupling constant made in this study may be rather approximate.

Gor'kov's approach to explaining superconductivity in $SrTiO_3$ [88] was criticized in Refs [100, 101]. In principle, this criticism can be extended to Refs [86, 87] dealing with superconductivity in FeSe/STO. At the same time, the use of phenomenological values of dielectric permeabilities at the FeSe/STO interface in [86, 87] makes the arguments reported in Refs [100, 101] only partly relevant for this case.

Finally, we can mention the recent rather detailed review of experiments on intercalated $A_xFe_2Se_2$ type systems [102].

References

1. Ginzburg V L *Contemp. Phys.* **9** 355 (1968); *Usp. Fiz. Nauk* **95** 91 (1968)
2. Ginzburg V L *Sov. Phys. Usp.* **13** 335 (1970); *Usp. Fiz. Nauk* **101** 185 (1970)
3. Ginzburg V L *Sov. Phys. Usp.* **19** 174 (1976); *Usp. Fiz. Nauk* **118** 315 (1976)
4. Ginzburg V L, Kirzhnits D A (Eds) *High-Temperature Superconductivity* (New York: Consultants Bureau, 1982); Translated from Russian: *Problema Vysokotemperaturnoi Sverkhprovodimosti* (Moscow: Nauka, 1977)
5. Sadovskii M V *Phys. Usp.* **51** 1201 (2008); *Usp. Fiz. Nauk* **178** 1243 (2008)
6. Ishida K, Nakai Y, Hosono H *J. Phys. Soc. Jpn.* **78** 062001 (2009)
7. Johnson D C *Adv. Phys.* **59** 83 (2010)
8. Hirschfeld P J, Korshunov M M, Mazin I I *Rep. Prog. Phys.* **74** 124508 (2011)
9. Stewart G R *Rev. Mod. Phys.* **83** 1589 (2011)
10. Kordyuk A A *Low Temp. Phys.* **38** 888 (2012); *Fiz. Nizk. Temp.* **38** 1119 (2012)
11. Mizuguchi Y, Takano Y *J. Phys. Soc. Jpn.* **79** 102001 (2010)
12. Sadovskii M V, Kuchinskii E Z, Nekrasov I A *J. Magn. Magn. Mater.* **324** 3481 (2012)
13. Nekrasov I A, Sadovskii M V *JETP Lett.* **99** 598 (2014); *Pis'ma Zh. Eksp. Teor. Fiz.* **99** 687 (2014)
14. Bozovic I, Ahn C *Nature Phys.* **10** 892 (2014)
15. Vivanco H K, Rodriguez E E *J. Solid State Chem.* **242** 3 (2016); arXiv:1603.02334
16. Guo J et al. *Phys. Rev. B* **82** 180520(R) (2010)
17. Yan Y J et al. *Chin. Sci. Rep.* **2** 212 (2012)
18. Hatakeda T et al. *J. Phys. Soc. Jpn.* **82** 123705 (2013)
19. Burrard-Lucas M et al. *Nature Mater.* **12** 15 (2013)
20. Lu X F et al. *Nature Mater.* **14** 325 (2015)
21. Pachmayr U et al. *Angew. Chem. Int. Ed.* **54** 293 (2015)
22. Lynn J W et al. *Phys. Rev. B* **92** 060510(R) (2015)
23. Nejadsattari F, Stadnik Z M *J. Alloys Comp.* **652** 470 (2015)
24. Wang Q-Y et al. *Chin. Phys. Lett.* **29** 037402 (2012)
25. Ge J-F et al. *Nature Mater.* **14** 285 (2015)
26. Miyata Y et al. *Nature Mater.* **14** 775 (2015)
27. Zhou G et al. *Appl. Phys. Lett.* **108** 202603 (2016); arXiv:1512.01948
28. Peng R et al. *Nature Commun.* **5** 5044 (2014)
29. Ding H et al. *Phys. Rev. Lett.* **117** 067001 (2016); arXiv:1603.00999
30. Song C-L et al. *Phys. Rev. B* **84** 020503(R) (2011)
31. Liu X et al. *J. Phys. Condens. Matter* **27** 183201 (2015)

32. Kuchinskii E Z, Sadovskii M V *JETP Lett.* **91** 660 (2010); *Pis'ma Zh. Eksp. Teor. Fiz.* **91** 729 (2010)
33. Skornyakov S L et al. *Phys. Rev. B* **80** 092501 (2009)
34. Nekrasov I A, Pavlov N S, Sadovskii M V *JETP Lett.* **102** 26 (2015); *Pis'ma Zh. Eksp. Teor. Fiz.* **102** 30 (2015)
35. Nekrasov I A, Sadovskii M V *JETP Lett.* **93** 166 (2011); *Pis'ma Zh. Eksp. Teor. Fiz.* **93** 182 (2011)
36. Shein I R, Ivanovskii A L *Phys. Lett. A* **375** 1028 (2011)
37. Nekrasov I A, Pchelkina Z V, Sadovskii M V *JETP Lett.* **88** 144 (2008); *Pis'ma Zh. Eksp. Teor. Fiz.* **88** 155 (2008)
38. Zhao L et al. *Phys. Rev. B* **83** 140508(R) (2011)
39. Nekrasov I A, Pavlov N S, Sadovskii M V *JETP Lett.* **97** 15 (2013); *Pis'ma Zh. Eksp. Teor. Fiz.* **97** 18 (2013)
40. Nekrasov I A, Pavlov N S, Sadovskii M V *JETP* **117** 926 (2013); *Zh. Eksp. Teor. Fiz.* **144** 1061 (2013)
41. Nekrasov I A, Pavlov N S, Sadovskii M V *JETP Lett.* **95** 581 (2012); *Pis'ma Zh. Eksp. Teor. Fiz.* **95** 659 (2012)
42. Nekrasov I A, Pavlov N S, Sadovskii M V *JETP* **116** 620 (2013); *Zh. Eksp. Teor. Fiz.* **143** 713 (2013)
43. Yi M et al. *Phys. Rev. Lett.* **110** 067003 (2013)
44. Niu X H et al. *Phys. Rev. B* **93** 054516 (2016)
45. Nekrasov I A, Sadovskii M V *JETP Lett.* **101** 47 (2015); *Pis'ma Zh. Eksp. Teor. Fiz.* **101** 50 (2015)
46. Niu X H et al. *Phys. Rev. B* **92** 060504(R) (2015)
47. Nekrasov I A, Pavlov N S, Sadovskii M V, Slobodchikov A A *Low Temp. Phys.* **42** 891 (2016); *Fiz. Nizk. Temp.* **42** 1137 (2016); arXiv:1605.02404
48. Liu D et al. *Nature Commun.* **3** 931 (2012)
49. Lee J J et al. *Nature* **515** 245 (2014)
50. Zhao L et al. *Nature Commun.* **7** 10608 (2016)
51. Fu H, Reich K V, Shklovskii B I *JETP* **122** 456 (2016); *Zh. Eksp. Teor. Fiz.* **149** 530 (2016)
52. Zhou Y, Mills A J *Phys. Rev. B* **93** 224506 (2016); arXiv:1603.02728
53. Chen M X, Agterberg D F, Weinert M, arXiv:1603.03841
54. Shaolong H et al. *Nature Mater.* **12** 605 (2013)
55. He J et al. *Proc. Natl. Acad. Sci. USA* **111** 18501 (2014)
56. Mizuguhci Y et al. *Supercond. Sci. Technol.* **23** 054013 (2010)
57. Kuchinskii E Z, Nekrasov I A, Sadovskii M V *JETP Lett.* **91** 518 (2010); *Pis'ma Zh. Eksp. Teor. Fiz.* **91** 567 (2010)
58. Miyata Y et al. *Nature Mater.* **14** 775 (2015)
59. Wen C H P et al. *Nature Commun.* **7** 10840 (2016)
60. Ye Z R et al., arXiv:1512.02526
61. Zheng F et al. *Phys. Rev. B* **93** 075428 (2016)
62. Shiogai J et al. *Nature Phys.* **12** 42 (2016)
63. Hanzawa K et al. *Proc. Natl. Acad. Sci. USA* **113** 3986 (2016); arXiv:1508.07689
64. Lei B et al. *Phys. Rev. Lett.* **116** 077002 (2016)
65. Barzykin V, Gor'kov L P *JETP Lett.* **88** 131 (2008); *Pis'ma Zh. Eksp. Teor. Fiz.* **88** 142 (2008)
66. Kuchinskii E Z, Sadovskii M V *JETP Lett.* **89** 156 (2009); *Pis'ma Zh. Eksp. Teor. Fiz.* **89** 176 (2009)
67. Chen X et al. *Phys. Rev. B* **92** 224514 (2015)
68. Kuchinskii E Z, Sadovskii M V *Physica C* **470** S418 (2010)
69. Sato T et al. *Phys. Rev. Lett.* **103** 047002 (2009)
70. Sekiba Y et al. *New J. Phys.* **11** 025020 (2009)
71. Fan Q et al. *Nature Phys.* **11** 946 (2015)
72. van Benthem K, Elsässer C, French R H *J. Appl. Phys.* **90** 6156 (2001)
73. Müller K A, Burkard H *Phys. Rev. B* **19** 3593 (1979)
74. Koonce C S et al. *Phys. Rev.* **163** 380 (1967)
75. Lin X et al. *Phys. Rev. X* **3** 021002 (2013)
76. Allender D, Bray J, Bardeen J *Phys. Rev. B* **7** 1020 (1973)
77. Inkson J C, Anderson P W *Phys. Rev. B* **8** 4429 (1973)
78. Uspenskii Yu A, Zharkov G F *Sov. Phys. JETP* **38** 1254 (1974); *Zh. Eksp. Teor. Fiz.* **65** 2511 (1974)
79. Allender D, Bray J, Bardeen J *Phys. Rev. B* **8** 4433 (1973)
80. Choudhury N et al. *Phys. Rev. B* **77** 134111 (2008)
81. Lee D-H, arXiv:1508.02461
82. Danylenko O V et al. *Eur. Phys. J. B* **9** 201 (1999)
83. Kulić M L *AIP Conf. Proc.* **715** 75 (2004)
84. Rademaker L et al. *New J. Phys.* **18** 022001 (2016)
85. Wang Y et al. *Supercond. Sci. Technol.* **29** 054009 (2016); arXiv: 1602.00656
86. Gor'kov L P *Phys. Rev. B* **93** 060507(R) (2016)
87. Gor'kov L P *Phys. Rev. B* **93** 054517 (2016)
88. Gor'kov L P *Proc. Natl. Acad. Sci. USA* **113** 4646 (2016); arXiv: 1508.00529
89. Wang S Q, Mahan G D *Phys. Rev. B* **6** 4517 (1972)
90. Nozières P, Schmitt-Rink S *J. Low. Temp. Phys.* **59** 195 (1985)
91. Randeria M, in *Bose–Einstein Condensation* (Eds A Griffin, D W Snoke, S Stringari) (Cambridge: Cambridge Univ. Press, 1995) p. 355
92. Lubashevsky Y et al. *Nature Phys.* **8** 309 (2012)
93. Kasahara S et al. *Proc. Natl. Acad. Sci. USA* **111** 16309 (2014)
94. Chubukov A V, Eremin I, Efremov D V *Phys. Rev. B* **93** 174516 (2016); arXiv:1601.01678
95. Shi X et al., arXiv:1606.01470
96. Rebec S N et al., arXiv:1606.09358
97. Zhang S et al. *Phys. Rev. B* **94** 081116(R) (2016); arXiv:1605.06941
98. Kulić M L, Dolgov O V, arXiv:1607.00843
99. Wang Y et al. *Phys. Rev. B* **93** 134513 (2016); arXiv:1602.03288
100. Ruhman J, Lee P A, arXiv:1605.01737
101. Klimin S N et al., arXiv:1606.00644
102. Krzton-Maziopa A et al. *J. Phys. Condens. Matter* **28** 293002 (2016)